DEPARTMENT OF PHYSICS
UNIVERSITY OF JYVÄSKYLÄ
RESEARCH REPORT No. 14/2006

DEVELOPMENT OF TRAP-ASSISTED SPECTROSCOPY AND ITS APPLICATION TO BETA DECAY OF NEUTRON-RICH ZIRCONIUM ISOTOPES

BY
SAMI RINTA-ANTILA

Academic Dissertation
for the Degree of
Doctor of Philosophy

To be presented, by permission of the
Faculty of Mathematics and Natural Sciences
of the University of Jyväskylä,
for public examination in Auditorium FYS-1 of the
University of Jyväskylä on December 18, 2006
at 12 o'clock noon

Jyväskylä, Finland
December 2006

ISBN 978-951-39-3178-0

URN:ISBN:978-951-39-3178-

Preface

The work reported in this thesis was carried out during the years 2000–2006 at the Department of Physics of the University of Jyväskylä. The whole staff has contributed to the pleasant working atmosphere of the department and deserves thanks for that. Especially, I would like to thank the staff of the mechanical and electronics workshops for the realization of the needed equipment, the cyclotron staff for the professional operation of the machine and secretaries for their helpfulness.

I would like to thank my supervisors Professor Juha Äystö and Docent Ari Jokinen for the opportunity to work in the group and for their guidance and support. Working in the IGISOL group has been lots of fun thanks to all its members. In particular, I would like to thank few past members of the group, Dr. Jussi Huikari, Dr. Arto Nieminen, Dr. Veli Kolhinen and Dr. Kari Peräjärvi for the great times. The expertise and help of the trap group, especially Mr. Tommi Eronen, Mr. Viki-Veikko Elomaa, Ms. Ulrike Hager, Mr. Jani Hakala, Dr. Stefan Kopecky, Mr. Juho Rissanen and Dr. Jerzy Szerypo are highly acknowledged. Warmest thanks to Dr. Iain Moore for using his time to read through my manuscripts.

The financial support from the Rector of the University of Jyväskylä, from the graduate school in particle and nuclear physics, and from the Waldemar von Frenckell's foundation are gratefully acknowledged.

I want to express my gratitude to my parents and my sisters for all the support and encouragement. Finally, I would like to thank my wife Katja for her understanding, support and love and my daughter Aivi for putting all these things in perspective.

Jyväskylä, December 2006

Sami Rinta-Antila

Abstract

Trap-assisted spectroscopy utilizes modern ion trapping techniques to manipulate low-energy radioactive ion beams in order to improve the experimental conditions for decay spectroscopy. In this thesis, two types of trap-assisted spectroscopy techniques were developed for the Penning trap system JYFLTRAP at the Ion Guide Isotope Separator On-Line (IGISOL) facility at the Accelerator laboratory of the University of Jyväskylä. In the first technique, the Penning trap purifies the sample of radioactive isotopes for the subsequent spectroscopic studies. It was shown that such a purification is feasible even for the most exotic isotopes accessible at IGISOL. In a commissioning experiment the Penning trap was used in a post-trap β-decay study of the neutron-rich zirconium isotopes ^{100}Zr, ^{102}Zr and ^{104}Zr. The comparison of the Gamow-Teller strength distributions obtained from this beta decay study, and theoretical calculations, point to a prolate deformation of these nuclei. In the second technique, the radiation emitted in the decay process of a trapped ion is recorded with a detector placed outside of the trap. Such a technique is called in-trap spectroscopy. The feasibility of in-trap conversion electron spectroscopy was first tested using REXTRAP at ISOLDE, CERN after which the tests were carried on at Jyväskylä using JYFLTRAP. An improved line shape in the spectra and an increased efficiency were obtained with this technique. The mass measurement capability of the JYFLTRAP system was employed to determine the masses of neutron-rich zirconium and niobium isotopes. The preparation Penning trap was used in the first direct mass measurement of $^{96-104}$Zr, of which the mass of ^{104}Zr was experimentally determined for the first time. The experimental two-neutron separation energies were compared to the global mass models of astrophysical interest, resulting in a notable discrepancy around the N=60 subshell closure. The masses of ^{100,102,104}Nb were measured with the precision trap. For ^{100}Nb and ^{102}Nb the masses of both the ground and excited isomeric states were measured.

Contents

1 Introduction

A variety of particle traps are widely used to study a range of physical phenomena. During the past 20 years this field has been honored by the highest recommendation. H.G. Dehmelt and W. Paul were awarded the Nobel prize in 1989 for the development of ion trapping techniques. Then in 1997, S. Chu, C. Cohen-Tannoudji and W.D. Phillips received the Nobel prize for the cooling and trapping of atoms using laser light. More recently, the studies of Bose-Einstein condensation using these optical and magnetic traps yielded the Nobel prize for E.A. Cornell, W. Ketterle and C.E. Wieman in 2001.

The advantage of a trap is that it provides a sensitive way of studying only one or a few particles at a time. Traps can also be used to select only particles that have the desired properties. Moreover, traps can be used to manipulate ensembles of trapped particles, namely cooling, moving, expanding, compressing and so on. In particular, Penning traps are suitable for mass measurements. Presently the most precise measurements of particle masses are done usin the Penning trap. A variety of techniques are in use however the common feature is that the mass is determined from the characteristic frequency of the particle motion in the trap.

For the above mentioned reasons the nuclear physics field utilizes traps for various purposes. Atomic masses and other properties of stable isotopes are measured with high precision to extract information on nuclear and atomic properties. However, to study comprehensively nuclear properties it is not enough to limit the measurements to the stable nuclei found in nature but one needs access to the radioactive isotopes. Radioactive ion beams are produced in two types of facilities. The first are the fragment separators which utilize high-energy heavy-ion beam fragmentation in light targets and subsequent in-flight separation of the fragments. This technique provides fast beams of even the shortest-living species. The second method is an isotope separator on-line (ISOL) technique in which a proton beam induced breakup of a heavy target nucleus is typically used as a production method. The products are then stopped, re-ionised, accelerated to a few tens of keV energy and mass separated. ISOL facilities have been a natural environment for experiments using traps as they require a low energy and high quality radioactive ion beam for their injection. Therefore it is not surprising that the pioneering on-line Penning trap mass spectrometer ISOLTRAP [1] was built at ISOLDE, CERN. However, lately the development of stopping techniques for fragment separator facilities have enabled the conversion of a

high energy radioactive ion beam into high quality low energy beam. Following this development – or in fact many cases triggering it – trap experiments have spread to these facilities. Examples of these experiments are SHIPTRAP at GSI, Germany [2] and LEBIT trap at NSCL/MSU, USA [3].

The mass determination has been the primary motivation of the use of Penning traps in nuclear physics. However, in the recent years the beam preparation traps have become more widely used, not simply for the purification of an ion beam prior to a precision mass measurement. For example the beam manipulation capabilities are used in decay and laser spectroscopy experiments. Collinear laser spectroscopy benefits from the bunched beam with a small energy spread, provided by a linear Paul trap. The mass selectivity of a Penning trap can be used to clean the unwanted species out of the radioactive ion sample, in preparation for decay spectroscopy. This beam manipulation is a very important part of the trap-assisted spectroscopy even though the term "trap-assisted" probably first brings to mind spectroscopy done inside the trap.

In nuclear physics the first results from in-trap spectroscopy have been obtained using optical traps. They are used to study beta-neutrino correlations by detecting the beta particle and the recoil ion with detectors placed facing the trapped atom cloud. These experiments are usually performed using magneto-optical traps (MOT) for example at Berkeley [4] and at TRIUMF, Vancouver [5]. Other variants of the MOT exist, such as additional time-orbiting-potential (TOP) trap as used in Los Alamos [6]. However, the optical traps are very dependent on the properties of chemical elements and therefore ion traps have been designed for similar beta-neutrino correlation experiments. For example, the WITCH experiment at ISOLDE, CERN [7] uses a Penning trap to prepare and to hold the decaying source for the beta-neutrino correlation measurement. For the same purpose a transparent Paul trap LPCTrap at GANIL, France has been built [8]. The fact that the trapped particles provide a material-free source that can be kept almost at rest inside a well-defined, small volume with relatively weak trapping fields makes these in-trap experiments attractive. Not only are these dedicated experiments designed to study extremely weak phenomena but also more standard nuclear spectroscopy could benefit from the ideal source provided by a trap.

The two aspects of trap utilization in nuclear spectroscopy, in-trap spectroscopy and spectroscopy with purified beams, are dealt with in this thesis, in addition to a small side trip to precision mass measurements.

The experimental work presented in this thesis has been carried out at ISOLDE, CERN and at the accelerator laboratory of the University of Jyväskylä (JYFL). At ISOLDE the first feasibility tests of in-trap conversion electron spectroscopy were performed using the REXTRAP accumulator and buncher Penning trap of the REX-ISOLDE post accelerator facility. The author of this thesis was responsible for the electron transport efficiency simulations and took part in the planning and carrying out of the on-line experiment. The main part of this thesis work is connected to the JYFLTRAP system at the IGISOL facility, JYFL. The author was strongly involved in the designing, building and commissioning of the JYFLTRAP Penning traps. From the beginning the trap

design was aimed to serve for two purposes, beam purification for spectroscopy and high-precision mass measurements. In fact the first masses were measured using only the purification trap. These included the neutron-rich zirconium isotopes $^{96-104}$Zr. An equally important function of the JYFLTRAP system is to act as a high resolving power mass separator for the nuclear spectroscopy experiments. The spectroscopy with purified beams is discussed in connection with the neutron-rich zirconium beta decay study. The in-trap conversion electron spectroscopy test was repeated at JYFLTRAP and some new results from that experiment are discussed in this thesis.

This thesis is based on the following enclosed publications:

1. In-trap conversion electron spectroscopy
   L. Weissman, F. Ames, J. Äystö, O. Forstner, K. Reisinger and S. Rinta-Antila
   Nuclear Instruments and Methods in Physics Research A 492, 451-463 (2002).

2. JYFLTRAP: a cylindrical Penning trap for isobaric beam purification at IGISOL
   V.S. Kolhinen, S. Kopecky, T. Eronen, U. Hager, J. Hakala, J. Huikari, A. Jokinen, A. Nieminen, S. Rinta-Antila, J. Szerypo and J. Äystö
   Nuclear Instruments and Methods in Physics Research A 528, 776-787 (2004).

3. Direct mass measurements of neutron-rich zirconium isotopes up to ^{104}Zr
   S. Rinta-Antila, S. Kopecky, V.S. Kolhinen, J. Hakala, J. Huikari, A. Jokinen, A. Nieminen, J. Äystö and J. Szerypo
   Physical Review C 70, 011301 (R) (2004).

4. Decay study of neutron-rich zirconium isotopes employing a Penning trap as a spectroscopy tool
   S. Rinta-Antila, V.-V. Elomaa, T. Eronen, U. Hager, J. Hakala, A. Jokinen, P. Karvonen, H. Penttilä, J. Rissanen, T. Sonoda, A. Saastamoinen and J. Äystö
   Submitted to European Physical Journal A.

2 Theoretical background

2.1 Physics of neutron-rich nuclei

The physics of neutron-rich nuclei is very rich in phenomena. Unlike the neutron-deficient side of the valley of β-stability where the Coulomb repulsion between protons limits the proton excess, the neutron-rich limit depends only on the proton-neutron asymmetry. Therefore, the neutron drip line is pushed much further away from the line of stability. Partly for this same reason, the neutron drip line has been experimentally probed only up to A $\sim$ 30 whereas the proton drip line which in fact crosses the N=Z line around Z=50 has been reached at much higher mass number. The majority of the "Terra Incognita" – the unknown land – of the chart of nuclei lies between the experimental limits of the known nuclei and the neutron drip line.

The large N/Z ratio gives rise to interesting nuclear matter behavior such as the neutron halo, seen for example in ^{11}Li [9], or in heavier systems a neutron skin in general. Experimentally, although more challenging than probing the charge distribution, many methods are used for probing the neutron distribution, see for example [10]. The neutron skin is defined only as an excess of neutrons over protons on the nuclear surface, whereas an extra requirement for the neutron halo phenomenon is a tail in the neutron distribution due to loosely bound low-ℓ neutrons surrounding a core. The understanding of the neutron skin can yield information about neutron stars as the same pressure of neutron-rich matter affecting the neutron skin thickness defines the radius of the neutron star [11]. Furthermore, an additional reason for interest in the neutron-rich nuclei within the astrophysical community is the rapid neutron capture process (r-process) which is believed to be responsible for the production of half of the elements heavier than iron. The r-process follows a path in which the neutron separation energy is about 2 – 3 MeV [12, 13]. Experimentally this path has been reached in only a few places and therefore it is a challenge for the theoretical work to successfully model the nuclei along this path. As the experiments push closer to the site of the r-process path, the theoretical extrapolations become smaller and thus the results of theory are more reliable. The main parameters needed to simulate the r-process are the nuclear masses, the β-decay half-lives and the Q_β-values. Related to the modeling of these nuclei, the changes of shell structure is predicted by self-consistent calculations. For example, the debated quenching of the N=82 shell gap far from stability [14] and the opening of a

new N=70 gap around Z=40 are predicted [15]. This change of shell structure is also an interesting phenomenon to be probed experimentally. The signature of a change in shell structure can be seen for example in the trend of the two-neutron separation energies or in the behavior of excited states.

2.2 Nuclear structure models

The history of nuclear models starts from a simple liquid drop model (LDM) first suggested by G. Gamow [16]. It is based on a short-range attractive interaction between the nucleons and combined with the nucleon fermionic nature (repulsive at very short distance) results in a rather constant nuclear matter density and binding energy per nucleon. The liquid drop model describes, quite successfully, the bulk nuclear properties varying smoothly as a function of nucleon number. However, the discovery of anomalies occurring in the observed nuclear data in the set of neutron and proton numbers led to a pursuit for and finally a formulation of a nuclear shell model [17, 18]. When the early simple shell model could only describe the nuclei close to the magic numbers, there was an alternative approach provided by the geometric models [19]. These models were in a sense built on top of the liquid drop model by allowing additional degrees of freedom, such as vibrations or rotations (associated with static deformation). Somewhere in the middle ground between the shell model and collective model there exists an algebraic approach [20]. In the following subsections the models relevant for this work are shortly introduced.

2.2.1 Nuclear shell model

The foundation of the nuclear shell model is built upon an assumption that each nucleon moves independently in a central potential created by the other nucleons. In the simplest case a harmonic potential can be used resulting a set of degenerate levels. However, the obtained magic numbers are not correct. The potential can be made more realistic by imitating the nuclear matter density distribution which leads to a potential having a finite depth, a flat bottom and a surface part where the potential gradually vanishes. This has the effect of decreasing the level of degeneracy by separating the states with a different ℓ quantum number, however is not enough to match the shell gaps with the empirical observations. The needed component to reproduce the observed magic numbers 2, 8, 20, 28, 50, 82 and 126 is a strong attractive spin-orbit component which splits the levels with $\ell \geq 1$ into two, such that the level with a larger j value is lower in energy. The relevant part of the single particle shell model levels for this work is presented in fig 2.1. With the independent particle model only the nuclei with a magic number of protons and neutrons can be described. This model also assumes a spherical nucleus which is of course true in the vicinity of closed shells. However, to broaden the applicability of the shell model the residual interaction between the nucleons above the closed shell – or core as it is usually referred – is needed to be taken into account (sometimes more active

shells are needed to explain observed properties *e.g.* superdeformation [21]). As the computing power has increased in recent decades larger and larger valence spaces can be calculated. However, the limit is still somewhere in the *pf(g)* shell ($N, Z \leq 50$). One way of proceeding from here is to use the Monte-Carlo Shell Model (MCSM) [22]. It reduces the dimensions of the basis by successive trials of different basis states and by selecting from those only the vectors that have an important contribution to the state of interest.

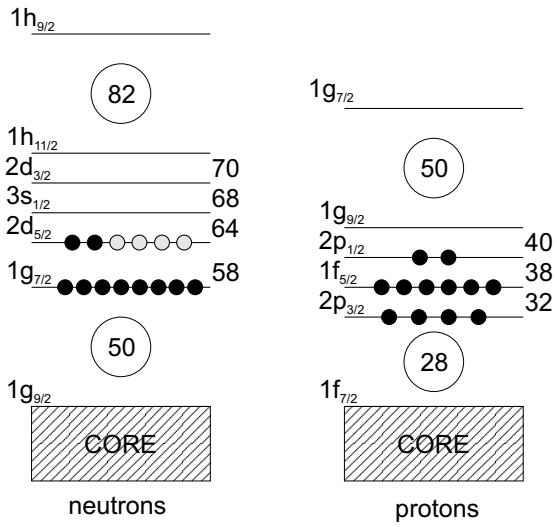

Figure 2.1: Schematic view of the shell model energy levels relevant for this work. The occupation of levels marked with black circles represents ^{100}Zr. The additional grey circles are neutrons of ^{102}Zr and ^{104}Zr.

2.2.2 Nilsson model

When the nucleus is no longer spherical the shell model potential must be deformed. In the Nilsson model [23, 24] deformation is introduced in a non-self-consistent way by fixing the deformation beforehand and calculating the single particle levels arising from that deformation. The deformation breaks the symmetry and the $(2j+1)$ degeneracy of the spherical states. The component of j along the symmetry axis, Ω, is used to label the states. It has values ranging from $-j$ to $+j$ but as a result of the reflection symmetry levels with $+\Omega$ and $-\Omega$ have the same energy *i.e.* the degeneracy is two. The levels are labeled in the Nilsson model as $\Omega^{\pi}[Nn_z\Lambda]$, where π is the parity obtained from $(-1)^N$, N is the principal quantum number, n_z is the principal oscillatory number along

the symmetry axis (the number of nodes) and Λ is the projection of the orbital angular momentum onto the symmetry axis. In the Nilsson model the shape of a deformed nucleus is parametrised by ϵ_λ parameters but often another β_λ parametrization related to deformed Woods-Saxon potential is used. In this parametrization the nuclear surface is described as

$$R(\theta, \beta) = C(\beta) R_0 \left[1 + \sum_\lambda \beta_\lambda Y_{\lambda 0} \right] \tag{2.1}$$

where C is a normalization factor needed to conserve the nuclear volume, R_0 is the radius of a corresponding spherical nucleus ($r_0 A^{1/3}$) and $Y_{\lambda\mu}$ are spherical harmonics. The transformation between these two parametrizations is possible but not trivial [25]. For small deformation an approximation $\epsilon_2 \approx 0.95\beta_2$ can be used. For an oblate deformation ($\beta_2 < 0$) the states with higher Ω are more bound and thus are lower in energy whereas in prolate deformation ($\beta_2 > 0$) it is the other way around. The levels cross at β_2=0 where they correspond to spherical single particle levels, see fig. 2.2.

2.2.3 Unified model

The unified model by Bohr *et al.* [19] describes nuclei in a more geometrical way and unites the underlying liquid drop model with the shell model. In particular, it gives a simple explanation for the excited states of the even-even nuclei where rotation-like or vibration-like patterns can be seen.

2.2.4 Algebraic model

Another kind of approach is taken in the interacting boson model (IBM). In this model the valence space is taken from the shell model but based on the strong pairing between similar nucleons the pairs of nucleons (or holes) are treated as interacting s and d bosons. This results in an U(6) symmetry group which can be reduced to an O(3) angular momentum conserving subgroup via three different paths: U(5), O(6) or SU(3). These correspond to the vibrator, transitional and rotor in the geometrical picture, respectively. The improved IBM-2 model separates neutron and proton degrees of freedom. A thorough introduction to the interacting boson model can be found in [27].

2.3 Beta decay

The nuclear beta decay is a weak interaction process in which a neutron is converted into a proton or the other way around. The underlying process at a more fundamental level is a conversion of an up quark into a down quark or *vice versa* by the emission of a $W^\pm$ boson. The boson mediating the weak force, in turn, decays immediately into two leptons, a positron and a neutrino or an electron and an antineutrino. Different coupling constants and operators

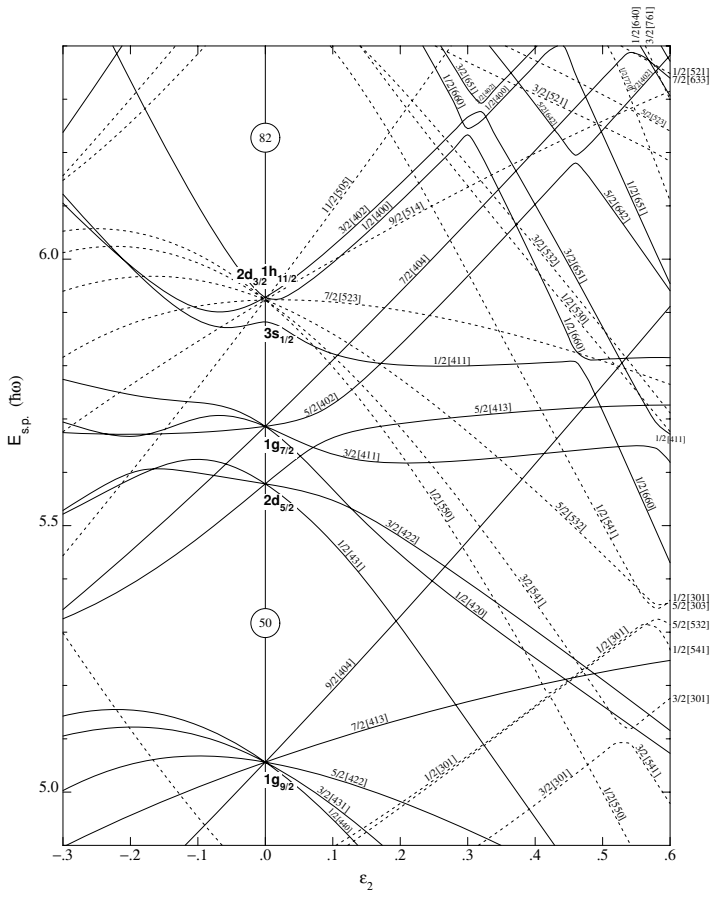

Figure 2.2: Nilsson diagram for neutrons $50 \leq N \leq 82$ [26].

involved in the standard electroweak model and the limits that can be set to these based on β-decay data are discussed in a recent review article ref. [28].

In a nuclear perspective, the beta decay can be divided into three types; β^-, β^+, and electron capture. The first decay increases the proton number and decreases the neutron number whereas the two latter decays decrease the proton number and increase the neutron number.

The available decay energy, defined as the mass difference between the mother and daughter nuclei, sets the β-decay window i.e. which states in the daughter nucleus are accessible for the β-decay. This energy is usually given in a form of a decay Q-value, which is the total kinetic energy available for the final state. In each isobaric chain there is one or more β stable nuclei which are more bound than their neighboring nuclei. In the chart of nuclides they form

a valley of beta stability, towards which the other nuclei β-decay. This work concentrates on the neutron-rich side of the valley where the decay Q-value is positive for the β^- decay. In the β^- decay a neutron is converted into a proton and from the available decay energy an electron and an antineutrino are created. The residual energy is converted into the kinetic energy of the e^- and $\bar{\nu}$ (the small recoil energy of the nucleus is neglected here even though it can be detected in dedicated experiments). Because there are two emitted particles the experimentally detectable kinetic energy, carried by the electron, has a distribution instead of a single energy peak. The decay Q-value can be determined from the maximum energy of this distribution, also known as the beta-endpoint. This information can be used to derive the mass difference between the parent and daughter nucleus. In fact, the majority of the experimentally determined masses on the neutron-rich side of the valley of stability have been obtained this way. Only recently Penning trap results have started to change this picture.

Based on the angular momentum carried by the electron and antineutrino in their total spin, the beta decay can be divided into two types, Fermi and Gamow-Teller decay. In Fermi decay the spins of the emitted leptons are antiparallel and in the Gamow-Teller decay they are parallel. These can be further divided in to classes of different forbiddenness depending on the angular momentum carried by the leptons. In table 2.1 the selection rules of the beta decay are summarized.

Table 2.1: Beta decay selection rules and typical logft values from ref. [29]

Transition type	log ft	L	Fermi		Gamow-Teller	
			ΔJ	$\Delta\pi$	ΔJ	$\Delta\pi$
Allowed	<5.9	0	0	no	0, 1	no
1st forbidden	>6.0	1	(0), 1	yes	0, 1, 2	yes
2nd forbidden	>10.6	2	(1), 2	no	2, 3	no

The selection rules given in table 2.1 can be used directly in the case of a spherical nucleus. However, if the nucleus is well-deformed as is the case with neutron-rich zirconium isotopes one has to consider the Nilsson states which are labeled with asymptotic quantum numbers, see 2.2.2. There are additional selection rules related to this set of quantum numbers and the transitions fulfilling the requirement $\Delta\Omega = 1$, $\Delta N = 0$, $\Delta n_z = 0$ and $\Delta\Lambda = 0$ are called allowed unhindered decays and typically they can be identified from $\log ft \leq 5$.

The transition probability can be derived from the Fermi Golden Rule. According to this rule the beta decay can be treated as a small pertubation that causes the nucleus to change from the initial state to the final state. In general the rate depends on the strength of the coupling and the number of possible

final states. The transition probability can be written in the form

$$\lambda = \frac{2\pi}{\hbar}\langle M_{if}\rangle^2 \rho(E_f) \tag{2.2}$$

where $\langle M_{if}\rangle$ is the matrix element of the interaction connecting the initial and final states and $\rho(E_f)$ is the density of the final states.

As the beta decay rate is proportional to the fifth power of the transition energy it is convenient to use the comparative half-life ft, where the phase-space factor f contains the energy dependence. Therefore, the ft value itself depends mainly on the nuclear matrix elements $\langle M_{if}\rangle$. In the allowed decay the following equation can be derived for the ft value.

$$ft = \frac{C}{\langle M_F\rangle^2 + (\frac{G_A}{G_V})^2\langle M_{GT}\rangle^2} \tag{2.3}$$

Here the nuclear matrix element is split into two parts Fermi $\langle M_F\rangle$ and Gamow-Teller $\langle M_{GT}\rangle$. G_A/G_V is the ratio of the axial vector and vector coupling constants and C is a constant. The numerical value for $|G_A/G_V| = 1.2695(29)$ given by the particle data group [30] is deduced from the measurements of the free neutron lifetime and the beta asymmetry coefficient of the neutron decay. This value is used later in the calculations. However, different numerical values are obtained if the allowed beta decay data of several pure GT and Fermi decays are also included in the fit. Furthermore, the value depends on the model assumptions and the number of fitted parameters. In ref. [28] values based on eight different model cases are given. The value for the constant C is obtained from the superallowed Fermi $0^+ \rightarrow 0^+$ β-decay $\mathcal{F}t$ value. Based on the recent compilation by Hardy and Towner [31] its value is 6147.0(2.4) s. In table 2.1 typical logft values for different kinds of transitions are given.

2.3.1 GT strengths

In Gamow-Teller decay both spin and isospin are changed and therefore the GT operator is referred to as $\sigma\tau$. In a simple single-particle estimate with an inert core the square of the Gamow-Teller matrix element for the allowed case is

$$\langle\sigma\tau\rangle^2 = 6(2j_f+1)\left\{ \begin{array}{ccc} \frac{1}{2} & \frac{1}{2} & 1 \\ j_i & j_f & \ell \end{array} \right\}^2 \tag{2.4}$$

In this work the following definition for the pure Gamow-Teller strength is adopted

$$B(\mathrm{GT}) = \langle\sigma\tau\rangle^2 = \frac{1}{ft}\frac{C}{(G_A/G_V)^2}, \tag{2.5}$$

where t is the partial half-life obtained from the total half-life T divided by the beta branching in question, and the values for C and G_A/G_V are given above.

The total GT-strength is defined as the sum of all individual transition strengths

$$B_\Sigma(\mathrm{GT}) = \sum_i B_i(\mathrm{GT}). \tag{2.6}$$

2.3.2 Models calculating β-decay properties of neutron-rich nuclei

The applicability of the shell model is limited to lower values of N and Z nuclei than the region of interest in this work due to the present computing capacity. Some shell model calculations can be performed however, for example, in the vicinity of the doubly-closed shell nucleus ^{132}Sn. In general though, for the mid-shell nuclei such as the neutron-rich zirconium isotopes a different approach has to be taken. Typically a mean field framework is adopted. In this method the basis is calculated using either Hartree-Fock (HF) with a possible additional BCS extension or the Hartree-Fock-Bogolyubov (HFB) method. The configuration mixing of the obtained basis states is then performed with one of the following: the Tamm-Dancoff Approximation (TDA), the Random Phase Approximation (RPA) or their respective quasiparticle versions QTDA and QRPA. When the initial state and all final states are created with these methods the transition probabilities can be calculated by the application of relevant transition operators. For the GT-transition they are of the form $\sigma\tau$ as discussed above. For example, a QRPA model used to calculate β-strength functions using single-particle levels and wave functions is introduced in ref. [32]. Another model, discussed later, uses a Skyrme type Hartree-Fock calculation together with TDA or RPA to derive the GT-strengths [33]. A pedagogical approach to microscopic nuclear theory including beta decay and configuration mixing can be found in ref. [34].

2.4 Internal conversion

Internal conversion is a process that deexcites the nuclear excited states. In this process the nuclear transition energy is given to one of the bound electrons of the atom. The kinetic energy of the electron depends on which atomic shell it was emitted from in the following way:

$$T_{e^-} = (E_i - E_f) - B_n, \tag{2.7}$$

where E_i and E_f are the energies of the nuclear initial and final states and the B_n is the binding energy of the emitted electron.

The ratio of the internal conversion intensity divided by the γ-ray intensity is called the internal conversion coefficient (ICC) (or just conversion coefficient for short). When both initial and final states have spin and parity of 0^+ a single electromagnetic transition is impossible, and only an internal conversion can take place (if the transition energy is above 1022 keV then an internal pair formation competes with IC). The ICC increases with higher Z, a decreasing transition energy, and an increasing transition multipolarity. The total ICC can be divided into subgroups depending on which atomic shell the electron was emitted from.

In this work the detection of electrons is of interest, therefore other processes following internal conversion and involving the emission of electrons have to be

considered. Two types of processes are discussed in the following sections.

2.4.1 Shakeup and shakeoff

When the central potential that the atomic electrons occupy suddenly changes due to the emission of an inner shell electron, the electrons have to reorganize themselves into new eigenstates. This rearrangement may involve the excitation of electrons to higher energy levels or even an ejection to the free electron state. These two cases are called shakeup and shakeoff, respectively. The former could be experimentally visible in the form of satellite peaks below the conversion electron peak as the shakeup takes place at the expense of the energy of the conversion electron. However, the number of emitted electrons and the ion charge state is unchanged. In the shakeoff a part of the conversion electron energy is given to the shakeoff electron. In the energy spectrum this shows up as a shakeoff continua close to zero energy and complementary shakeoff satellites below the conversion electron peak. The probability of an inner shell shakeoff electron following an internal conversion is very small of the order of a few 10^{-4} for Z$\sim$50 [35]. However, the probability of the removal of an outer shell electron is much higher.

2.4.2 Auger electron emission

When a vacancy is created in the inner shell of an atom, it will be quickly filled by an electron from an outer shell. The excess energy can be released in the form of electromagnetic radiation *i.e.* an X-ray, or it can be given to one of the outer shell electrons which is emitted. This latter process results in what is commonly known as an Auger electron. The kinetic energy of an Auger electron can be calculated from the electron binding energies

$$T_{e_A} = B_V - B_F - B_E, \tag{2.8}$$

where B_V is the binding energy of the shell with the initial vacancy, B_F is the binding energy of the shell from which the electron moves to fill the vacancy, and B_E is the binding energy of the shell from which the Auger electron is emitted. Following this process there are two vacancies in the electron shells which are subsequently filled from the outer shells and again either X-rays or Auger electrons are emitted. A cascade of Auger electrons following a vacancy in an inner shell can leave the atom highly charged. It has been shown that the average charge state of an ion after undergoing this kind of a cascade is equal to the number of electron shells [36]. In a solid material the electron cloud of an atom is quickly recharged but if the ion is created in a vacuum the high charge state can survive for a considerable length of time.

2.5 Nuclear mass models

One key property of the ground state of a nucleus is its mass. The mass is often referred to as the atomic mass which can be experimentally determined.

The atomic mass is derived from the nuclear mass and the masses and binding energies of the atomic electrons

$$M_{at}({}^{\mathrm{A}}_{\mathrm{Z}}\mathrm{El}) = M_{nuc}({}^{\mathrm{A}}_{\mathrm{Z}}\mathrm{El}) + Z \cdot m_e - \Sigma B_e/c^2, \tag{2.9}$$

where the M_{at} is the atomic mass, M_{nuc} the nuclear mass of the same isotope, m_e the electron mass and ΣB_e the total binding energy of all the electrons. If the mass is measured with sufficient precision the atomic binding effects become non-negligible. This precision is seldom reached however with atoms of radioactive isotopes. The main component of the total mass – the nuclear mass – is a result of the masses of the constituent nucleons and the nuclear binding energy

$$M_{nuc}({}^{\mathrm{A}}_{\mathrm{Z}}\mathrm{El}_{\mathrm{N}}) = Z \cdot m_p + N \cdot m_n - B({}^{\mathrm{A}}_{\mathrm{Z}}\mathrm{El}_{\mathrm{N}})/c^2, \tag{2.10}$$

where $B({}^{\mathrm{A}}_{\mathrm{Z}}\mathrm{El}_{\mathrm{N}})$ is the nuclear binding energy. This final term in (2.10) contains all the relevant nuclear physics information. m_p and m_n are the masses of the free proton and neutron, respectively. The atomic mass is often given in the form of a mass excess which is the difference between the mass number multiplied by the atomic mass unit and the real mass of the atom

$$ME({}^{\mathrm{A}}_{\mathrm{Z}}\mathrm{El}) = A \cdot u - M_{at}({}^{\mathrm{A}}_{\mathrm{Z}}\mathrm{El}), \tag{2.11}$$

where the atomic mass unit $u = M_{at}({}^{12}C)/12$.

The evolution of the mass unit together with a historical view on nuclear masses and mass spectrometry can be found from ref. [37]. A recent review article on mass spectrometry with stored ions gives an overview of the development of the experimental methods and includes examples of applications of precise mass information needed in different fields of physics [38].

The importance of understanding the mass of the nucleus has been the driving force behind a vast number of theoretical models. The following sections give a short overview of the different models describing the mass of a nucleus. A recent review article on nuclear mass determination gives, in addition to an introduction to the experimental techniques, an extensive overview of the present mass models on the market [39]. In the more recent article of Pearson and Goriely [40] the Hartree-Fock-Bogolyubov models of the Brussels group are compared with three other mass models, in particular for their suitability towards astrophysical purposes.

2.5.1 Macroscopic models

The first semiempirical mass formula that attempted to describe the nuclear binding energy was that of C.F. von Weizsäcker [41]. The formula was based on the liquid-drop model of the nucleus, with a volume term, a surface term, a Coulomb term accounting for the Coulomb repulsion between the protons and a symmetry term to favor nuclei with N=Z. Later on a surface-symmetry term was added resulting in the following form for the nuclear binding energy [39]

$$E = a_{vol}A + a_{sf}A^{2/3} + \frac{3e^2}{5r_0}Z^2A^{-1/3} + (a_{sym}A + a_{ss}A^{2/3})\left(\frac{N-Z}{A}\right)^2 \tag{2.12}$$

This simple five-parameter model reproduces the gross behavior of the nuclear binding energy remarkably well although there is an obvious need for shell corrections due to large deviations near the closed shells. To take into account these microscopic effects some modifications were made to the liquid-drop model. This led to introduction of the microscopic-macroscopic, or in short, mic-mac models.

2.5.2 Microscopic-Macroscopic models

Myers and Swiatecki introduced the first set of microscopic corrections to the liquid drop model [42]. The shell effects were taken into account in the form of a bunching of levels for spherical nuclei whereas for deformed nuclei the bunching was assumed to vanish. This bunching was described by a simple shell function. Pairing energy was included by adding a term for odd-odd nuclei and subtracting the same term for the even-even nuclei. The extra binding binding at yhe N=Z line was accounted for by the addition of a Wigner term.

The present improved model of the Myers and Swiatecki model family is called the Finite-Range Droplet Model (FRDM). This includes Strutinsky shell corrections, BCS pairing corrections and a Wigner term. The macroscopic part has been upgraded to include, among others, finite range surface effects and an exponential compressibility term. The latest version is described in ref. [43]. As the experimental data is often compared to the FRDM it has been thoroughly analyzed in ref. [39], and was selected in the comparison of models in ref. [40].

The Extended Thomas-Fermi plus Strutinsky Integral ETFSI gives a close approximation to the Hartree-Fock method. In the ETFSI model the macroscopic part is calculated with a fourth-order extended Thomas-Fermi approximation using a Skyrme force. Following this, the same Skyrme force is used to calculate the microscopic part. Therefore the two parts have origin more common than the other mic-mac calculations. The latest form of this model ETFSI-2, can be found in ref. [44]. The results of this model, are very similar to those of the Hartree-Fock calculations [45].

The Thomas-Fermi model [46] is used to calculate the masses of 9000 isotopes. This model uses a different force and the calculation is only to zeroth-order compared to the fourth order extended Thomas-Fermi. The differences between these two models can be seen in the poorer representation of the nuclear surface when using the Thomas-Fermi model. In addition the shell corrections are taken from FRDM rather than being calculated self-consistently. Despite this, a good fit to the experimental data has been achieved, which may be due to the large number of parameters used in the model.

2.5.3 Microscopic models

The available fully microscopic models are based on an effective nucleon-nucleon interaction or a relativistic mean field (RMF). In the nonrelativistic approach the nuclear properties are calculated by the Hartree-Fock method usually using Skyrme- or Gogny-type forces. On top of the mean field picture there are still

some correlations not included in the HF-framework. One of them is pairing, which can be introduced to the model in two different ways, either by treating it with a BCS method after each iteration step or by including it in a fully variational way using the Hartree-Fock-Bogolyubov (HFB) method. The former works only close to stability, and for nuclei close to the neutron drip line the HFB method should be used [39]. Another correlation to be introduced separately is the Wigner term. Because this term is strongly localized around N=Z it can be taken into account by an additional Wigner energy of the form $E_W = V_W e^{-\lambda|\mathrm{N-Z}|/\mathrm{A}}$, simply added to the HF energy.

In the relativistic mean field method nucleons are represented by Dirac spinors and the interaction is mediated by mesons. However, the meson parameters are fitted to finite nuclei rather than nucleon-nucleon interaction. The merit of the RMF model is that it is Lorentz invariant and therefore the spin-orbit term is spontaneously created. Thus far the masses of only even-even nuclei have been calculated and with a very high rms error of 2.6 MeV [47]. A recent review on the applications of the self-consistent relativistic mean-field models is given in ref. [48].

The first complete mass table based on Hartree-Fock method was calculated using the HFBCS-1 mass formula by Goriely *et al.* [49]. The HFBCS-1 model treated the pairing in a BCS approximation. The first full HFB calculation HFB-1 [50] was followed shortly by HFB-2 [51] from the same group. The latest version of this model HFB-9 [52] has parameters fitted to a data set of 2149 measured masses found in the latest mass compilation [53]. According to the authors this latest model should be preferably used in the r-process calculations above all previous models including the ETFSI and HFBCS models by the same group [54]. In the latest model the root mean square deviation of the fit to 2149 masses is 0.733 MeV.

2.5.4 Other global models

The Duflo-Zuker model [55] lies between the fully microscopic and mic-mac models as it does not treat the nuclear interactions in a microscopic way, rather it uses "pseudopotentials". The Hamiltonian is divided into monopole and multipole parts of which the former gives the single particle properties whereas the latter is responsible for the residual interactions, including pairing and Wigner correlations. These terms are then parametrized and fitted to the existing data. There are two versions of these parameter sets, the original with 28 parameters and a later model simplified to only 10 parameters. Both sets were fitted to the AME1995 data with rms deviations of 375 keV and 506 keV, respectively. Duflo-Zuker is one of the models usually used for the astrophysical calculations due to a good agreement with the experimental data and a rather good predictive power.

The model by Koura *et al.* [56] (abbreviated as KTUY05 according to the last names of the authors) also has two parts similar to that of the mic-mac models although they are not identified in the same manner. The first part of the model gives the general trends about which the second part fluctuates. This

model has an improved even-odd term compared to the earlier KUTY00 model [57] from the same group, which is used in comparisons in refs. [39, 40].

2.5.5 Local mass models

The Interacting Boson Model is also used for mass determination but rather than a global fit the parameters are fitted for each studied region separately. An introduction to the nuclear binding energy derivation using this model and its application to nuclei in the 50–82 shell is given in ref. [58]. Inspired by the results of [Publication 3] the same model was used to calculate the energy spectra and two neutron separation energies of the neutron-rich zirconium isotopes [59].

3 Experimental techniques

3.1 ISOL method

The Isotope Separator On-Line (ISOL) technique was developed in the 1950s and 1960s to enable the study of short-lived rare isotopes. In the ISOL system reaction products produced in nuclear reactions are stopped, ionized and accelerated with electric fields to a few tens of keV, and are then mass separated with a magnetic field. The ability to ionize plays a crucial role in the ISOL performance. It often determines the efficiency, selectivity and ability to produce isotopes of certain elements. The target in which the reactions take place is usually an integrated part of the ion source. Either the target can be thick and act as a catcher material or it can be thin and followed by a separate solid or gaseous catcher. Figure 3.1 shows schematically different ways of stopping reaction products and preparing them for mass separation. With thicker targets the production yields are typically higher, but the extraction time of reaction products to the ion source is longer, and therefore the effective yield of very short-lived isotopes becomes smaller. In particular there is a group of elements, the so-called refractory elements, which are inaccessible for the thick target or solid catcher method due to their high boiling point. For example, the isotope separators ISOLDE at CERN and ISAC at TRIUMF, Vancouver, use thick targets and a selection of different ion sources to produce mass-separated low-energy radioactive ion beams. In section 3.1.1 the ISOLDE facility is described in more detail. The thin target and gas catcher method is used in Ion Guide Isotope Separator On-Line facilities all around the world, including Jyväskylä, where the method was first developed. The IGISOL facility at Jyväskylä is described in section 3.1.2.

3.1.1 ISOLDE

At ISOLDE [61] radioactive isotopes are produced in the fission, spallation and fragmentation of nuclei induced by 1–1.4 GeV proton pulses taken from the PS-Booster, a stack of four small synchrotrons. The repetition rate of the PS-Booster proton pulses is 1.2 s however only a selected number are directed to the ISOLDE target, the rest are sent to other experiments. Products from the proton-induced reactions are stopped inside a thick target. To release them out of the target matrix the whole target is heated to very high temperature. This

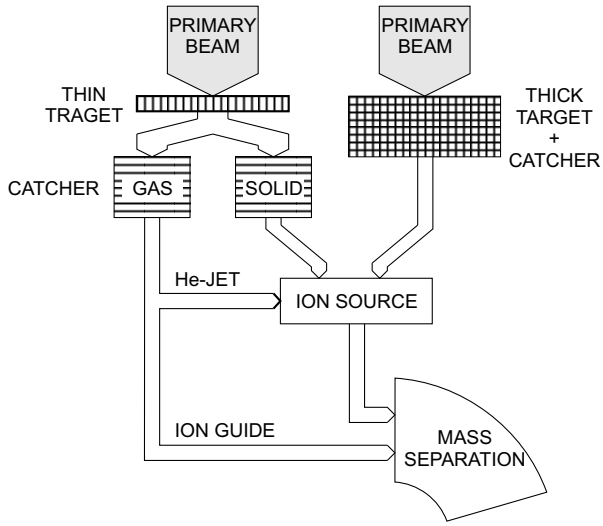

Figure 3.1: Schematic view of different ISOL concepts [60].

causes the radioactive atoms to diffuse out to the attached ion source, which can be one of three types. A surface ion source is the simplest type where the ionisation takes place on a hot surface of the transport line tube, made out of a material with a work function suitable for the element to be ionized. For example, a tube made out of tungsten or tantalum can be heated up to 2400 °C. A plasma ion source can be used for elements that can not be surface-ionized, for instance noble gases. Finally, the third type of the source is a Resonant Ionisation Laser Ion Source RILIS [62], which is similar in geometry to the surface ionisation source however the cavity is not kept at high temperature. Laser beams of up to three different wavelengths are used to excite a bound electron via intermediate levels to the continuum, *i.e.* to ionize the atom. This method of ionisation is highly selective, such that even different isomeric states can be favored in ionisation [63]. The only background contamination in RILIS comes from easily surface-ionized elements as the tube has to be slightly heated to prevent sticking of atoms on the surface. After ionisation ions are accelerated to 60 keV and mass separated with a dipole magnet. There are two separate target stations and separators available at ISOLDE. The General Purpose Separator GPS has a mass resolving power R=2400 while the High Resolution Separator HRS is routinely operated at R=5000 but in theory it should reach R=30000. These two separators can provide low energy radioactive beams of more than 850 isotopes to a wealth of experiments in the ISOLDE hall see fig 3.2.

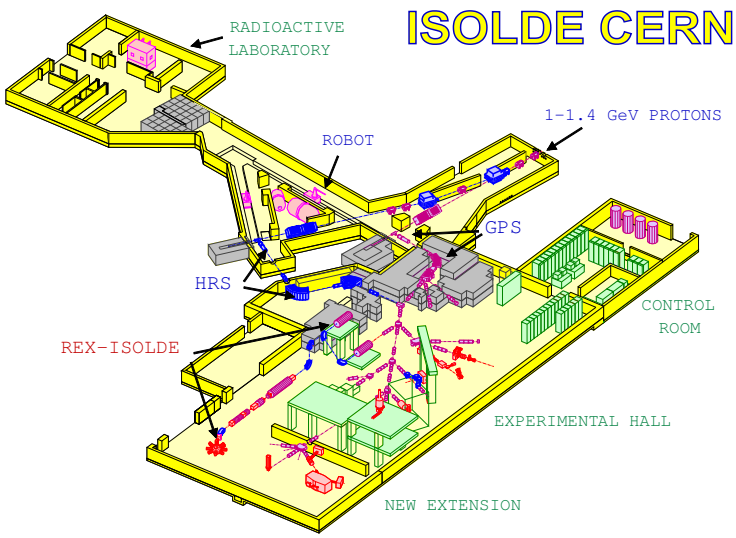

Figure 3.2: ISOLDE facility layout [64]

3.1.2 IGISOL

The Ion Guide Isotope Separator On-Line IGISOL technique was developed in Jyväskylä in the early 1980s [65, 66, 67, 68, 69]. The present layout of the IGISOL facility is shown in fig. 3.5. In the ion guide technique the reaction products recoiling out of a thin target are slowed down and thermalised in the buffer gas (typically helium or argon) as primary ions. The charge state of these ions gradually decreases due to collisions with the buffer gas atoms. Finally a considerable portion of the reaction products are thermalised in the buffer gas as singly charged ions. These ions are then swept out through an exit nozzle to an adjacent vacuum chamber by gas flow. When the ions exit the ion guide they are guided through a hole in a skimmer electrode with an electric field whereas the neutral buffer gas is mostly skimmed away. The ions are further accelerated to 30–40 keV energy and are sent into the separating magnet. A schematic view of the ion guide principle is shown in fig. 3.3. The combination of using a thin target and without the need for reionisation means that the IGISOL technique is chemically non-selective and faster compared to a conventional ISOL technique.

There are three main ion guide designs used for different production reactions. For light-ion induced fusion evaporation reactions a small volume (few cm^3), rotatable ion guide with two target positions is used. For heavy-ion induced fusion evaporation reactions a set of moving targets is placed some 10 cm upstream from a larger volume (100 cm^3) ion guide. The primary beam is stopped before a large area thin window on the guide by a small beam stop. The larger angular spread of the reaction products recoiling out of the target allow them to pass the beam stop and enter the guide through the thin window.

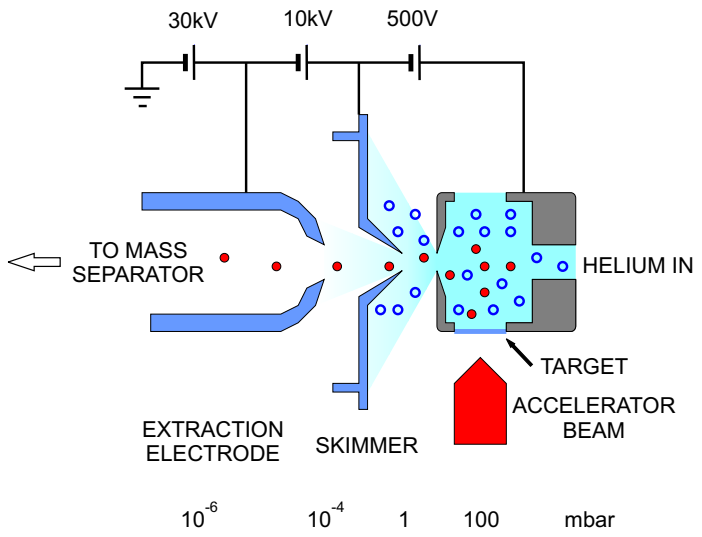

Figure 3.3: Ion guide operation principle with a skimmer-based extraction. Filled circles represent the reaction products recoiling out of the target and ending up as thermalised ions. Open circles are neutralized reaction products and buffer gas atoms. The volume surrounding the ion guide is evacuated with a Roots blower unit. Second differential pumping stages are evacuated with diffusion pumping units. Typical pressure ranges of different volumes are indicated below the drawing.

For the work in this thesis, a light-ion induced fission ion guide was used. Early fission experiments [70, 71] showed the strength of the IGISOL technique in the study of refractory fission products. The limit of known nuclei was reached in the mass region of A=106–118, and after that pushed further out towards the neutron drip line. The major differences in the design of the fission and the fusion ion guide result from different reaction kinematics. Unlike the fusion evaporation reaction where the products are recoiling from the target in the primary beam direction, the fission fragments are emitted isotropically at an energy of $\sim$ 100 MeV. This enables the use of a geometry where the beam impinges on a target in a volume that is separated from the stopping volume by a 1 mg/cm^2 nickel foil, see Fig. 3.4. This separation reduces the recombination of the reaction products that would be caused by the beam induced plasma. The target itself is a 15 mg/cm^2 thick sheet of natural uranium tilted to 7° with respect to the beam axis resulting in a 120 mg/cm^2 effective thickness. Fission is induced by 25–30 MeV protons with a typical intensity of between 5 and 10 μA.

Fission induced by an energetic proton has more symmetric mass distribution compared to thermal-neutron induced fission. In the neutron-induced fission the probability to produce symmetric A=105–125 fragments is three orders of magnitude smaller than to produce fragments around A=95 and A=140. In 30 MeV proton-induced fission the same ratio is a factor of two yielding higher production rates of transitional nuclei between A=100 and A=132.

In simulations a stopping efficiency of the order of 1% has been obtained for the fission ion guide [72, 60]. However, the experimental total efficiency is only of the order of 10^{-4} [60] leaving a few per cent survival of stopped ions in the gas volume and surviving transport through the separator. This low value is due to neutralisation losses in the plasma created by the fission fragments flying through the stopping volume and due to space-charge effects in the extraction region where ions are guided out of the stopping cell.

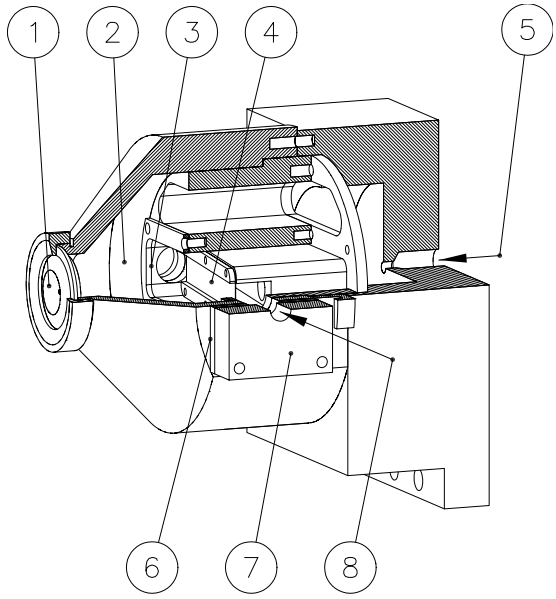

Figure 3.4: The fission ion guide used for the production of neutron-rich nuclei at IGISOL. The following parts are numbered in the figure 1) exit nozzle, 2) stopping volume, 3) separating foil, 4) tilted uranium target, 5) helium inlet, 6) beam window, 7) graphite collimator, 8) accelerator beam.

With an upgraded IGISOL front end the yields have been improved by factor of roughly three [73]. The main improvements were increasing the pumping speed in the extraction region and therefore enabling the use of a larger aperture in the extraction electrode and replacement of the skimmer electrode with a radio frequency sextupole ion guide (SPIG). A short description of the SPIG can be found in ref. [74]. The SPIG is also a part of a new laser ion source

system, called FURIOS [75] which aims for an improved selectivity and increased production yield in particular for the heavy-ion reactions.

The mass separation is done with a Scandinavian type 55° dipole magnet that has a tilted exit face for beam focusing. Its typical mass resolving power $R = M/\delta M$ is below 500 however it is sufficient to select a single mass number for the experiments. The mass resolving power depends on the front-end parameters such that when a higher energy spread is introduced to the beam due to increased gas cell pressure or higher electric fields used for extracting the ions, the mass resolving power decreases. However, the overall yield is generally directly proportional to these two parameters. Therefore, yield optimization has to be done at the cost of the mass resolving power or vice versa.

A beam switchyard equipped with a Faraday cup and a silicon detector for beam diagnostics is located at the separator focal plane. The separated beam can then be sent either straight to the central beam line or electrostatically deflected by 30° towards the trap beam line. The central beam line is typically used for normal decay spectroscopy set-ups. The transmission is good and the ion optics are easy to optimize.

A recent review article [76] describes the present status and applications of the IGISOL technique. A description of the IGISOL system in Jyväskylä can be found in ref. [77] and the latest upgrades in ref. [73].

3.2 JYFLTRAP

The JYFLTRAP system is a combination of a gas filled radio-frequency quadrupole for beam cooling and bunching and a double Penning trap for beam purification and precision mass measurements. In the following sections these devices are introduced. A brief introduction to the Penning trap operation principle is also given.

3.2.1 Radio-frequency quadrupole cooler and buncher

The use of electric fields to accelerate ions under poor vacuum between the ion guide exit hole and the skimmer electrode introduces some energy spread to the beam. To efficiently inject this beam into the Penning trap the energy spread has to be reduced and the continuous IGISOL beam has to be bunched. For this purpose a radio-frequency quadrupole (RFQ) cooler was designed and built in the IGISOL beam line. The RFQ cooler accepts the low quality ion beam and confines it in the radial direction with oscillating electric fields, see fig.3.6. This structure is filled with a low pressure (p=0.1 mbar) helium buffer gas in which the injected ions are thermalised. The rod electrodes are also segmented allowing an application of a DC potential that guides the ions to the extraction end of the structure. The beam is bunched by applying a pulsed voltage to the end plate electrode and accumulating ions in a potential well created by the DC fields. The ions are subsequently released in short bunches when the wall is lowered, see fig 3.7. The availability of a bunched beam enables an efficient

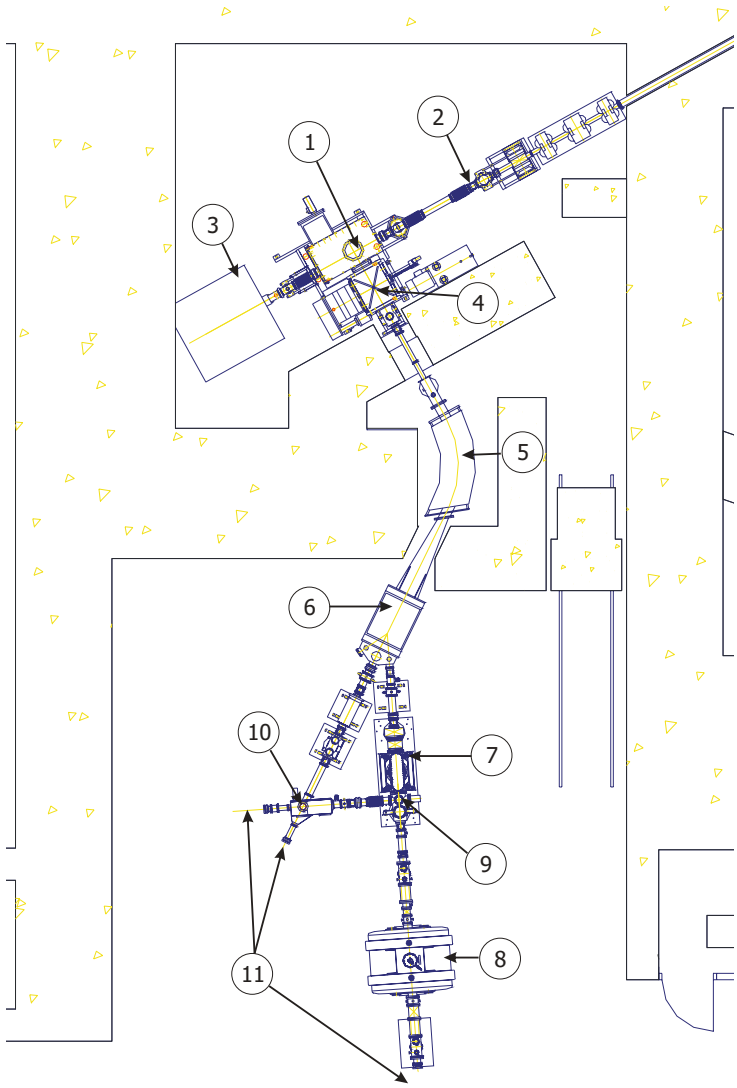

Figure 3.5: Layout of the IGISOL facility. The following parts are numbered: 1) target chamber, 2) primary beam line, 3) beam dump, 4) extraction chamber, 5) dipole magnet, 6) beam switch-yard, 7) RFQ cooler and buncher, 8) Penning traps, 9) 4-way quadrupole deflector, 10) beam line to collinear laser setup, and 11) possible detector set-up locations.

dynamic trapping scheme to be used for injection to the Penning trap. To avoid recreation of the energy spread when extracting from the cooler the ions are transported to high vacuum rather carefully inside a miniature RFQ before

acceleration. The RFQ cooler and buncher and its performance are described in refs. [78, 79].

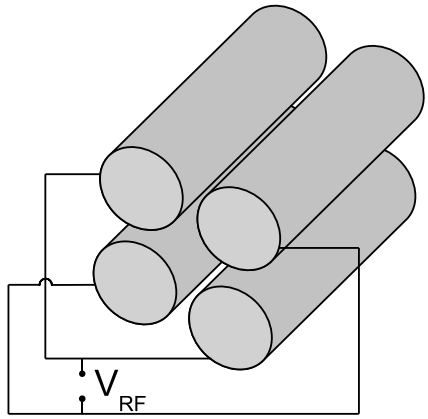

Figure 3.6: Radio-frequency quadrupole operation principle.

3.2.2 Penning trap operation principle

The Penning trap is an electromagnetic trap that confines charged particles by the combination of a strong homogeneous magnetic field and a static quadrupole electric field [80]. Axial confinement is achieved by the electric field and radial confinement by the magnetic field. Forces induced by these fields lead to three eigenmotions of the trapped charged particle, see fig 3.8. In the axial direction the particle undergoes a harmonic oscillation in a harmonic electric potential and in the radial plane there are two circular motions around the magnetic field lines, a slow magnetron motion and a fast reduced cyclotron motion with corresponding frequencies of ν_- and ν_+, respectively. The sum of these frequencies is the true cyclotron frequency ν_c which has the following relation to the mass m and charge q of the particle and to the magnetic field strength B

$$\nu_C = \nu_+ + \nu_- = \frac{1}{2\pi} \cdot \frac{q}{m} \cdot B. \tag{3.1}$$

A superconducting solenoid is used to produce a strong enough magnetic field for the Penning traps used in mass determination. Not only the strength but also the homogeneity of the field over the whole trapping volume is important, when measuring or exciting the frequencies of characteristic motions of the particles in the trap. The homogeneity ensures that the ions with different motion amplitudes feel the same field and that there is no variation due to different starting conditions. The higher order multipole imperfections can also

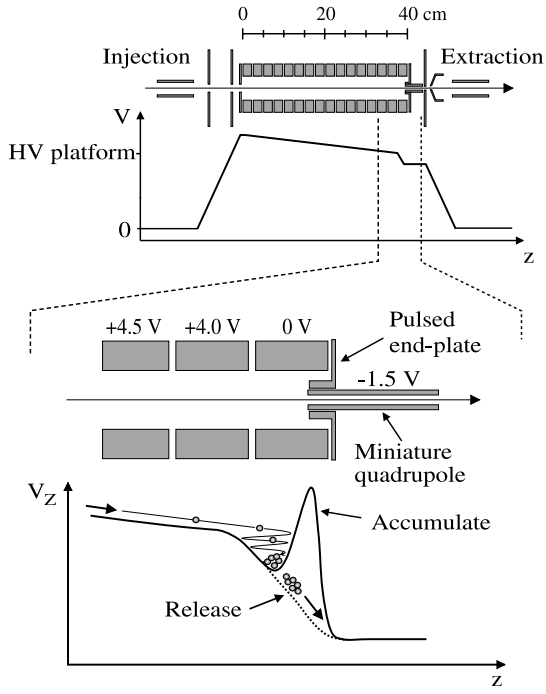

Figure 3.7: Bunching in the RFQ with a pulsed end plate electrode [79].

couple the different eigenmotions in an unwanted way. In practice the trap electrodes introduce some inhomogeneity due to the magnetic susceptibility of the material. Time-dependent fluctuations of the magnetic field are caused mainly by temperature and pressure changes in the trap environment. Temperature changes cause the magnetic susceptibility of the material surrounding the trap and trap electrodes to vary. Pressure changes outside the magnet on the other hand affect the pressure of the liquid nitrogen and helium vessels which may alter the magnetic field. These two effects can be minimized by stabilizing both the temperature in the warm bore of the magnet and the pressure in the helium vessel, as has been demonstrated at SMILETRAP [81]. Other time-dependent effects come from the slow change in the current of the superconducting magnet causing a slow linear drift in the field and possible movement of ferromagnetic objects in the vicinity of the magnet.

The quadrupole electric field is induced by applying static electric potentials to the trap electrodes. A simple way to produce the quadrupole field is to shape the electrodes so that their surfaces follow the equipotential lines. This means that the electrodes must be shaped as hyperboloids of revolution, forming two end-caps and a ring electrode see fig. 3.9 a). For a positively charged particle the trapping potentials in the electrodes are such that the ring electrode is at a

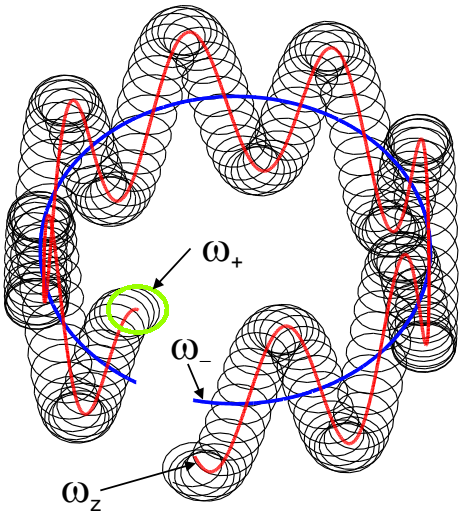

Figure 3.8: Three eigenmotions of an ion in a Penning trap. The reduced cyclotron motion, magnetron motion and axial oscillation are labeled by their angular frequencies ω_+, ω_- and ω_z, respectively.

lower potential with respect to the end-caps. This type of hyperboloidal trap is characterized by the parameters ρ_0 and z_0 which are the smallest inner radius of the ring electrode and half of the smallest distance between the end-caps, respectively. Using these parameters a characteristic trap dimension d can be derived.

$$d^2 = \frac{\frac{\rho_0}{2} + z_0^2}{2} \tag{3.2}$$

Usually traps are designed so that $z_0 = \rho_0/2$ leading to $d = z_0$ and a potential well depth in the z- direction $D_z = V_0/2$, where V_0 is the voltage applied between the ring and end-cap electrodes.

In practice the quadrupole field produced in this way has some imperfections due to the finite size of the electrodes. Additionally, there are small holes in the end-caps to inject and to extract particles from the trap. Therefore, some correction is needed and is done by introducing compensation electrodes between the end-cap and ring electrodes, and around the holes in the end-caps. Many Penning traps designed for precision work use this kind of electrode structure even though making hyperboloid shaped electrodes accurately enough is challenging. Effects of the above mentioned imperfections in the magnetic and electric fields are estimated in the case of ISOLTRAP in ref. [82].

Rather than having only a small hole in the end-cap for injection, an open ended electrode structure is sometimes desirable, for example to make the particle injection easier. This is achieved by using a cylindrical open end Penning

trap [83] in which all electrodes have the same inner diameter. Even with this shape of electrode geometry a relatively pure quadrupole field can be generated in the trapping volume close to the trap axis by applying suitable potentials to the long, tube-like end-caps and to the ring and compensation electrodes that have optimized lengths see fig. 3.9 b). This design was further improved by adding a second pair of compensation electrodes and optimizing the geometry when designing the new ISOLTRAP cooler trap [84]. A similar geometry was adopted to the Penning trap electrodes of the JYFLTRAP setup.

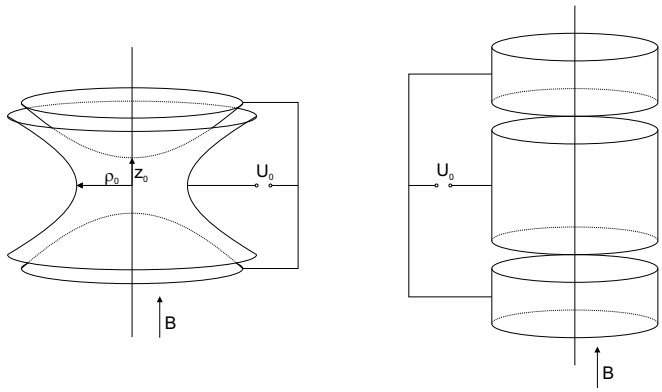

Figure 3.9: Hyperbolical and cylindrical Penning trap.

The radial motion of the trapped particle can be excited with time-varying azimuthal electric fields. In order to achieve this, the ring electrode is segmented or alternatively the segmentation is applied to the correction electrode between the end-cap and ring electrode. With a dipole field a single motion, either magnetron or reduced cyclotron motion, can be excited by applying the corresponding characteristic frequency. This dipole excitation increases the amplitude of the driven motion. Radial motions can also be coupled together by driving the particle motion with a transverse RF quadrupole field using the particle's true cyclotron frequency. Coupling these motions with this excitation converts one motion into the other and back again. One full conversion from one motion to another lasts

$$T_{conv} = \frac{\pi}{a_0}\frac{m}{q}(\omega_+ - \omega_-), \tag{3.3}$$

where a_0 is the strength of the driving electric field and therefore proportional to the amplitude of the RF voltage V_{RF} and ω_+ and ω_- are the angular frequencies

of the reduced cyclotron and magnetron motion, respectively. This conversion is illustrated in fig. 3.10. The driving of the ion motion from magnetron to reduced cyclotron motion can be done either quickly with a larger excitation amplitude or slowly with a small amplitude. However, this excitation time or observation time is inversely proportional to the resonance width. Therefore, with a longer excitation a better resolution can be obtained.

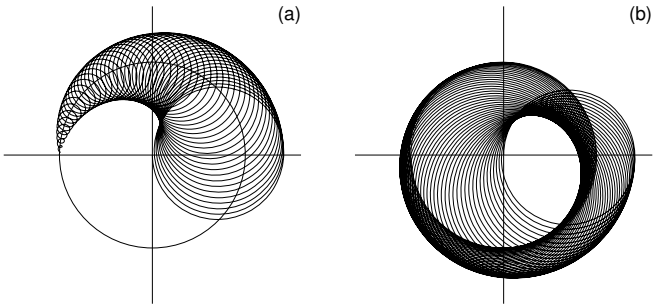

Figure 3.10: Conversion of pure magnetron motion to pure cyclotron motion when applying an azimuthal quadrupole excitation with the particle's true cyclotron frequency. For clarity the first half of the conversion is presented in the left panel and the second half in the right panel.

3.2.3 Purification trap

The purification trap is described in detail in [Publication 2]. However, a short description is given here as an introduction and to describe some details that have changed over the past two years. The two JYFLTRAP Penning traps are situated inside the warm bore of a 7 T superconducting solenoid built by Magnex Ltd. The magnet has two homogeneous regions 10 cm up- and downstream from the magnet center with homogeneities below 10^{-6} and 10^{-7} at the locations of the purification and precision trap, respectively. In the design, a cylindrical electrode geometry was adopted following the example of the ISOLTRAP cooling trap and REXTRAP. The dimensions and potentials were scaled to suit with the electrode inner radius of 16 mm that was preselected for JYFLTRAP [85].

The purification trap is buffer gas filled with a typical pressure of the order of a few times 10^{-5} mbar. The buffer gas is helium supplied by AGA and its purity level is 99.99990% (6.0). The gas pressure is adjusted with a needle valve and the feeding line pressure after the needle valve is monitored with two capacitive gauges covering the pressure range of $10^{-5} - 1100$ mbar. Buffer gas is fed into the trapping volume through a hole in the injection side end-cap electrode. The higher pressure region is delimited by a 4 mm diaphragm upstream and a 2 mm diaphragm downstream from the purification trap, see fig. 3.11.

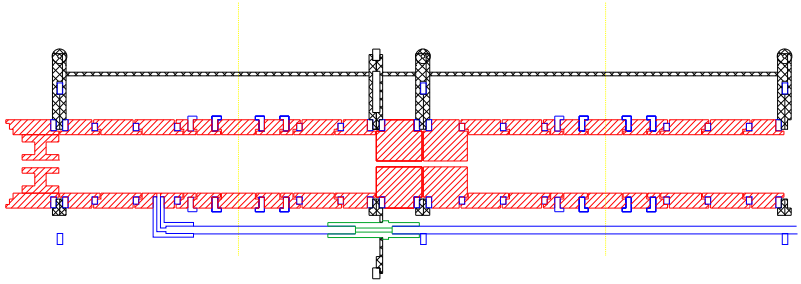

Figure 3.11: Axial cross section of the trap electrodes. Vertical lines indicate the centers of the traps. On the left is the purification trap and on the right the precision trap. The distance between the traps is 20 cm. This picture shows only the trap electrode sub-stacks, the rest of the electrode stack is left out.

The injection to the trap from the RFQ is pulsed which means that the initially lowered potential wall on the injection side is raised when the ion bunch is reflected from the extraction side wall. The trap potential is set so that the ion bunch arrives on the level of the potential well bottom and thus has the minimum amount of axial energy after the capture. The timing of the capture depends on the ion mass and it has been optimized for a few masses between which an interpolation can be used. However, as the bunch has a length in time and space a fraction of ions are lifted with the rising wall to higher energy. This extra energy has to be damped away in the buffer gas before further manipulation can be done. After this cooling period ions are situated axially in the center of the trap where the electric and magnetic fields have minimum distortions. Then a mass selective buffer gas cooling technique with a sideband excitation is performed [86]. Initially the radius of the magnetron motion of all trapped ions is increased above 1 mm by a dipole excitation with a mass-independent magnetron frequency. This excitation is followed by a quadrupole excitation with a mass-dependent cyclotron frequency which converts the slow magnetron motion of the selected ion species into a fast reduced cyclotron motion. This fast motion quickly loses its energy in collisions with the buffer gas atoms and the ions are centered on the trap axis. When the trapped ions are then ejected through a diaphragm with a 1 mm radius only the centered ones can pass. The mass resolving power of this method depends on the excitation time. With a shorter cycle time the resolving power is lower than with longer excitation and also a higher buffer gas pressure has to be used. However, the purification cycle with a higher resolution usually gives a lower transmission.

Typical scans of stable ^{124}Xe ions with different total cycle times are shown in fig. 3.12. The settings were not particularly optimized for these different cycles. One of the highest mass resolving powers obtained is for ^{58}Cu, with a MRP of 145,000, using a 450 ms total cycle time. On the other hand the

shortest purification cycle used was only 71 ms in total, and was used for decay spectroscopy of ^{62}Ga. The MRP was sufficient to separate ^{62}Ga from ^{62}Zn (difference in masses 9181 keV). If the half-life of the studied nucleus permits, the typical purification cycle is of the order of 200 ms. Then the required pressure in the trap is also lower than when using extremely short cycles. Although the traps are separated by a 5 cm long channel with 2 mm diameter, some buffer gas leaks into the precision trap. If higher pressure is needed in the purification trap it also affects the precision trap performance. This of course is not a problem when the purification trap is used on its own for beam purification.

3.2.4 Precision trap

The precision trap is used for mass measurements. It is operated in high-vacuum at a pressure of $\sim 10^{-8}$ mbar. The electrode geometry is the same as in the purification trap, see fig 3.11. The extraction side end-cap is followed by a 40 cm long drift tube with the same inner diameter as the trap electrodes. The acceleration back to the ground potential is done in a few steps. The injection from the purification trap is achieved with careful timing to minimize the energy given to the ion when closing the trap. The injection is followed by a dipole excitation with the magnetron frequency, where the phase-locking technique [87] is used. After the dipole excitation has increased the ion's magnetron radius the magnetron motion is converted into a reduced cyclotron motion by a quadrupolar excitation with ion's cyclotron frequency. This conversion increases the ion's radial energy as the ratio between the magnetron and reduced cyclotron frequency is 10^3 leading to an energy ratio of 10^6. When the ion is ejected this radial energy is converted into an axial energy as the magnetic moment related to the ion's radial motion interacts with the magnetic field gradient of the trap. The energy difference is detected with a micro-channel plate ion detector as a reduced time of flight when the ions are excited with the true cyclotron frequency. The difference in the time of flight between the off- and on-resonance ion is referred as the time-of-flight effect. For example, in fig. 3.13 the TOF effect is 250 μs or about 50 %. The method of cyclotron frequency detection with the time-of-flight technique is presented in ref. [88].

The total time of flight (typically few hundreds of μs) is dominated by the low energy drifting time before the extraction to 30 keV energy. After acceleration the ions can still be steered with an xy-deflector and focussed with an Einzel lens onto the ion detector. For the ion detection, a pair of multi-channel plates (MCP) in a chevron configuration are positioned at ground potential 1.5 m downstream from the precision trap. Due to the relatively high energy of the impacting ion a detection efficiency of around 60 % has been measured for the MCP detector. The signal from the MCP anode is amplified with an Ortec VT120 Fast Preamp and fed either directly into a multi-channel scaler (MCS) SR430 from Stanford Research Systems or via an Ortec Constant-Fraction Discriminator (CFD). The MCS is read out via GPIB connection to the PC running the control and scanning program. The same program controls the frequency generators used for the excitation, and the timing sequences for all time-dependent

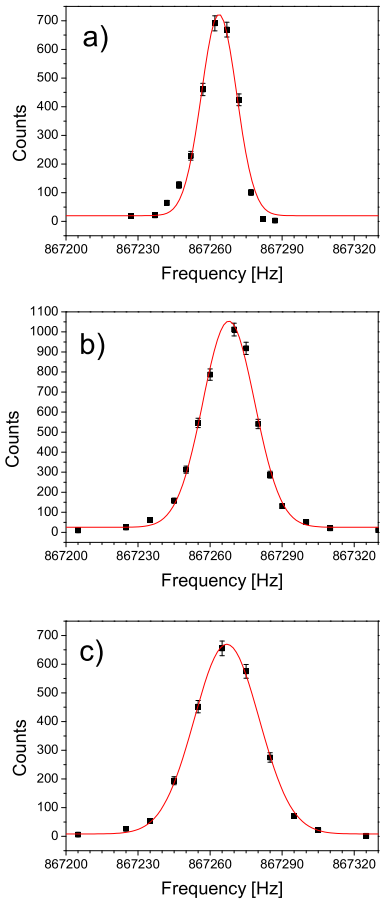

Figure 3.12: Example of the purification trap resolving power with different cycle times. ^{124}Xe ions a) 400 ms R=50000 b) 180 ms R=34000 c) 120 ms R=27000.

actions via a CAN bus and a timing card Pulseblaster PB24-100-32k, respectively. A second PC controls the DC voltage supplies (ISEG and Spellman) for all the trap and cooler electrodes as well as the ion optical elements in the trap beam line.

In the time-of-flight spectrum the average time of flight of the ions in some predefined time window is plotted against the excitation frequency, see fig. 3.13. The time window is selected such that it cuts away the ion counts that are clearly

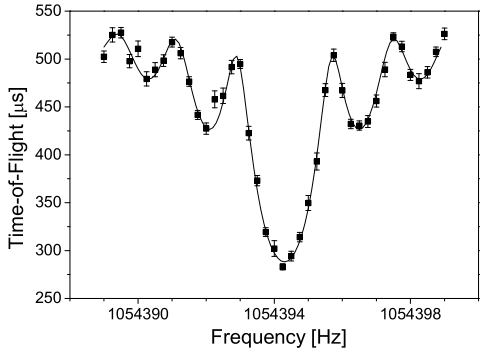

Figure 3.13: Time-of-flight resonance of stable ^{102}Ru obtained with a 600 ms excitation time in the precision trap.

not related to the studied ion. Typically the contaminants in the spectrum arrive much faster to the MCP than the studied ions and are related to the radioactive decay of the studied ion inside the trap. The amount of this fast background is proportional to the ratio of the trapping time to the decay half-life. The composition of this contaminant peak is either decay products in a higher charge state or lighter rest gas atoms ionised by the charge exchange with the decay products. An example of a raw plot of ion counts against the time of flight for ^{104}Nb and for stable ^{102}Ru is shown in fig. 3.14. In the spectrum of stable ^{102}Ru there are practically no counts below bin 320 as nothing decays in the second trap. As the time of fight for ^{104}Nb is similar the same bin 320 can be used as a lower limit for the analysis window.

Once the cyclotron frequency has been determined, equation 3.1 gives the relation to the unknown mass. As the magnetic field strength changes over time it has to be determined by a reference measurement of a well-known mass before and after the measurement of the mass of interest. By interpolating between the two reference measurements a reference cyclotron frequency ν_c^{ref} can be determined. The unknown mass can therefore be obtained by using the following equation

$$m_{un} = \frac{\nu_c^{ref}}{\nu_c^{un}}(m_{ref} - m_e) + m_e, \tag{3.4}$$

where m_{ref} is the mass of the reference atom and m_e the electron mass.

There have been some improvements done to the extraction electrode geometry compared to that presented in the thesis of V. Kolhinen [89]. The important changes are the splitting of the so-called plug electrode into two parts and the extension of the ground electrode inside the beam tube insulator. The plug electrode is the first electrode not attached to the trap electrode stack. Relative to the magnetic field it is situated where the field lines start to diverge strongly.

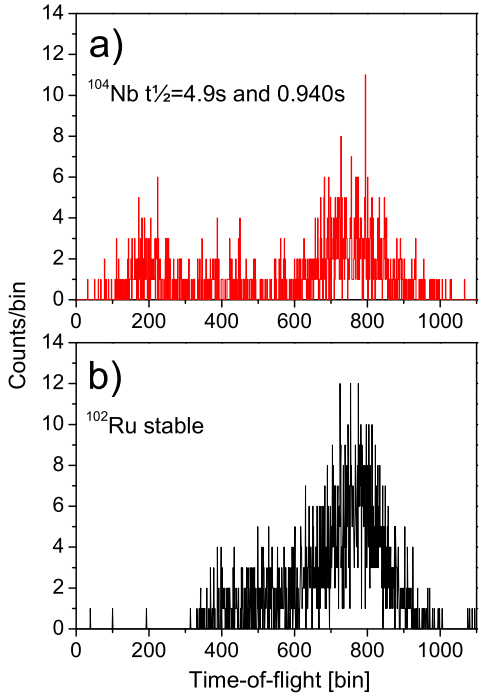

Figure 3.14: The upper panel shows ^{104}Nb ($t_{1/2}$ = 4.9 s and 0.94 s) and the lower panel the stable ^{102}Ru time-of-flight spectrum. The decay related fast component around bin 200 is missing from the spectrum of ^{102}Ru. The bin width is 640 ns.

The division of this electrode adds a new acceleration step and thus keeps the beam more focused when coming out of the high magnetic field, whereas the ground electrode elongation improves the shielding of the insulator from the beam. Related to the spectroscopy with purified beams an additional Einzel lens has been placed behind the MCP used for time-of-flight measurements to enable better focusing of the beam to the decay spectroscopy set-ups. A Faraday cup and a second MCP has been placed into a diagnostics chamber before a spectroscopy set-up, for trap and extraction line tuning.

3.3 Spectroscopy with purified beams

In this work the purification trap was used to provide monoisotopic samples of neutron-rich zirconium nuclei for decay spectroscopy study. The experiments are reported in [Publication 4]. In the following section some general comments

on purification cycle are made.

3.3.1 Purification cycle

The purification is done as explained in section 3.2.3. The precision trap potentials are set so that it merely acts as a drift tube for the bunch released from the purification trap. The timing cycles are prepared in such a way that the duty cycle is as large as possible. This means that the RFQ is collecting a new ion bunch from IGISOL while the previous bunch is being purified in the purification trap. The needed purification time is judged from the mass separation between the wanted species and the contaminant ions. An additional limit is set by the half-life of the nucleus. The transmission efficiency compared to the central beam line spectroscopy position has been 40% in maximum whereas more typical value is 20%.

A typical mass scan of fission products of mass A=100 in the first trap as detected by the MCP is shown in fig. 3.15. The cycle time in this scan was 370 ms. For the decay spectroscopy experiment the cycle time could be reduced to 180 ms and still having enough resolving power to resolve ^{100}Zr from ^{100}Nb.

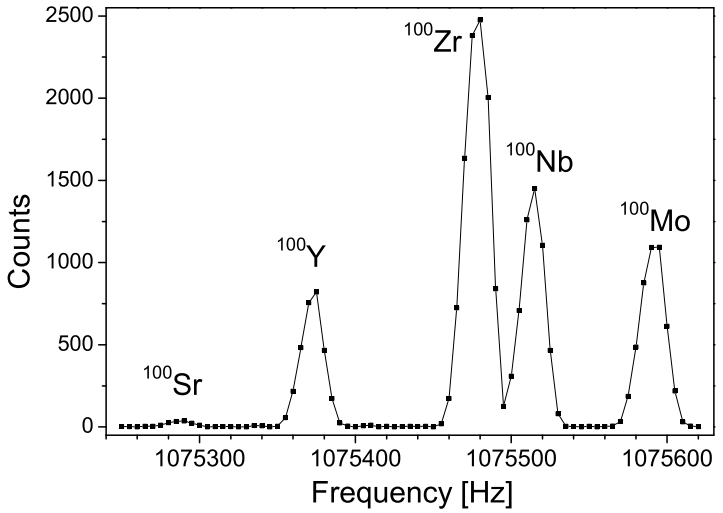

Figure 3.15: Mass scan of A=100 fission products in the purification trap. The used cycle time was 370 ms and the mass resolving power $R \sim 65000$.

The utmost care has to be taken when the purification trap is tuned for a spectroscopy experiment in order to avoid having beam of unwanted isobars

leaking through the trap. In a mass measurement virtually anything may happen outside the detection window of about 1 ms after the release from the second trap without any disturbance on the measurement. However in spectroscopy experiment isobaric leaks are unacceptable. When capturing the ion bunch arriving from the RFQ the rising injection wall may throw part of the bunch over the back wall if the timing is not perfect or if the actual bunch length is longer than the width of the trapping potential in the axial direction. This problem is more severe with a larger number of ions in the bunch as the release from the RFQ becomes slower due to space charge effects. It has been shown that the bunch width from the RFQ has a $N^{1/3}$ dependency on the number of ions in the bunch [90]. Furthermore, as the light ions move faster they fill a larger volume in space with the same time width and thus are harder to capture in the trap. To prevent lifting of the ions over the back wall the injection side potential wall is not lifted to the same level as the back wall but left 10 volts lower.

3.3.2 Detector set-up and acquisition

For the nuclear spectroscopy a detection set-up has been constructed at the end of the trap extraction line. It can basically be a normal decay spectroscopy set-up but some limitations come from the stray magnetic field of the superconducting magnet. At the end of the trap beam line the level of the stray field strength is 0.3 mT along the beam tube axis. This has been seen to disturb an ordinary unshielded photomultiplier (PM) tube. However, by selecting a PM-tube designed for use in a higher magnetic field and by using a mumetal shielding around the PM-tube, scintillator detectors can be used without a reduction in efficiency. Semiconductor detectors are not affected by this small field.

The zirconium decay study was done in two separate experiments. In both experiments the purified beam was implanted into a movable collection tape. The tape was always moved to a fresh point before starting the acquisition of a new isotope. Different detector set-ups were used for the two experiments. The first set-up was simply a large germanium γ detector and on the opposite side of the implantation point a planar 2 mm thick plastic scintillator for β detection was mounted, see fig. 3.16 a). For the second experiment the detector set-up was improved by replacing the planar scintillator with a cylindrical scintillator surrounding the implantation point. In addition a second large germanium detector and a low energy germanium detector (LEGe) were added, see fig. 3.16 b). In this new set-up the β detection efficiency increased by a factor of seven. Inclusion of the LEGe detector allowed detection of X-rays and low energy γ-rays that were found to be crucial in the determination of ground state feeding in the zirconium β-decay. In the first run the count rate was modest and a singles trigger was used. In the second experiment β- or LEGe-singles or $\gamma - \gamma$ coincidence triggered the acquisition. Data was collected in an event mode with the VME based IGISOL Data Acquisition (IDA). Each event was time stamped with the cycle time and the universal time both of them with a

millisecond resolution. The cycle time was reset at every release of the bunch from the purification trap. The measurement electronics is presented in fig. 3.17.

Spectroscopy data was collected in the Eurogam format. The event data was sorted using MTSort language. From the first experiment β-gated γ spectra were analyzed. From the May 2005 data 2D γ-γ and γ-LEGe matrices were created to find coincidences. Peak energies and areas were analyzed from β-gated γ data with the RADWARE package [91] and coincidences were sought with the MIDAS program.

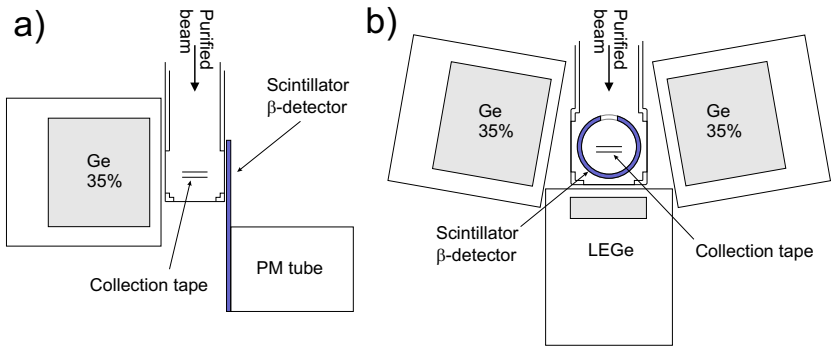

Figure 3.16: Layout of the detector set-ups a) used in the first zirconium experiment in 2004 and b) used in the second experiment in 2005.

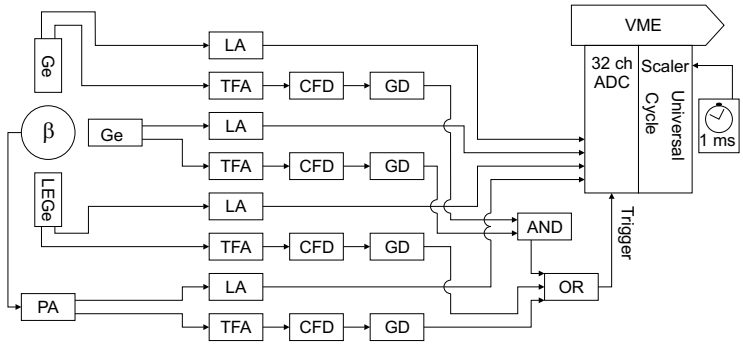

Figure 3.17: Flow diagram of the detection electronics of the second experiment. The following abbreviations are used: PA preamplifier, LA linear amplifier, ADC analog to digital converter, TFA timing filter amplifier, CFD constant fraction discriminator, GD gate and delay generator.

3.4 In-trap conversion electron spectroscopy

Traditionally conversion electron decay spectroscopy has been performed by using an implanted source placed in a solenoidal magnetic lens system to transport the electrons efficiently to a detector located at the other end of the magnet. An example of this kind of device is ELLI, a conversion electron transporter spectrometer at IGISOL [92]. The use of the magnetic field to transport electrons is needed to reduce the background introduced by the electromagnetic radiation. The detector can be placed far from the source reducing the solid angle for γ and X-rays whereas the electrons are focussed to the detector. However, the drawback of an efficient transport is that electrons that are emitted at large angles and have undergone multiple scattering are also transported to the detector. These scattered electrons are partly responsible for the complex line shape of a conversion electron spectrum, where a tail is seen on the low energy side. This complex line shape makes the analysis of the peak intensity and its position rather challenging [93].

3.4.1 A feasibility test at REXTRAP

REXTRAP is the first part of the REX-ISOLDE post-accelerator system for radioactive ions [94]. Normally it is used to accumulate, cool and bunch an ISOLDE beam before injecting it into an EBIS charge breeder. REXTRAP is a large-volume Penning trap filled normally with argon buffer gas. It is placed on a 60 kV high voltage platform to decelerate the ISOLDE beam. The trap is designed to hold large numbers of ions, even up to 10^7 ions can be delivered as cooled ion bunches [95]. The injection into the trap is done in a continuous manner. Therefore, there is a higher pressure region through which the ions must pass as they enter the trap. In this region they lose enough energy so as not to be able to overcome the injection potential wall after one reflection from the back wall. To separate the different pressure regions there are diaphragms providing differential pumping barriers in an otherwise 50 mm inner diameter trap electrode structure, see fig. 3.18. The harmonic trapping potential itself is situated in a lower pressure region. The trapped ion bunch can be mass-selectively cooled onto the trap axis as explained earlier in section 3.2.3.

REXTRAP was selected for the feasibility test of in-trap conversion electron spectroscopy because at that time it was easy to access and it was not yet needed for the main task of providing bunches for the post accelerator. The large inner diameter of the electrode structure made it rather easy to find a detector that could be installed in the available space.

3.4.2 In-trap detector

The requirements for the detector are partly technical related to the environment where it is used, and partly conceptual. As we are dealing with an ideal source the performance of the detector should be as good as possible to get the best out of the source. The presence of the buffer gas excludes cryogenic detectors and the

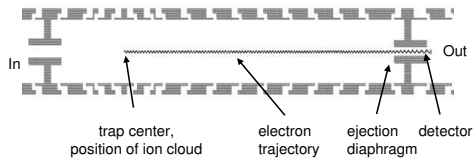

Figure 3.18: In-trap detector set-up in REXTRAP. The source ion is held in the trap and the emitted electrons are transported to the detector situated behind the diaphragm.

outer diameter of the assembly is limited by the electrode geometry. However the needed radius of the active area is quite small due to the strong magnetic field. A Canberra detector assembly EB10GC-500P and PA1201 preamplifier were selected for the tests. The detector itself is 500 micron thick with an active area of 10 mm^2 and dead layer of only 250 Å. In fig. 3.19 a photo of the detector in its holder is shown. The detector and the first stage amplification FET can be cooled with a peltier element to improve the resolution. However, this option was not used in these in-trap experiments.

Figure 3.19: In-trap detector in its holder.

3.4.3 In-trap spectroscopy at JYFLTRAP

At Jyväskylä the in-trap conversion electron spectroscopy test was performed employing the JYFLTRAP system and using the same detector as used at REXTRAP. Some modifications were made to the detector holder to enable the installation of a small movable Faraday cup (FC) in front of the silicon detector, see fig. 3.20. This FC served as a diagnostic tool for the trap tuning with a stable ion beam and it acted as a shield for the silicon detector from the high intensity beam.

The position of the detector in the on-line run is depicted in fig. 3.21. The detector holder was isolated from the vacuum chamber and it was floated at the potential of the last electrode of the trap electrode stack. Therefore, also the NIM rack for the detector electronics and the PC for data acquisition were lifted to this same potential. The acquisition PC was remotely operated from the ground potential via a fiber optical ethernet link.

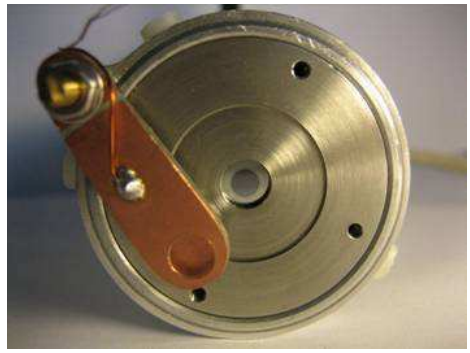

Figure 3.20: Front view of the in-trap detector and the movable Faraday cup.

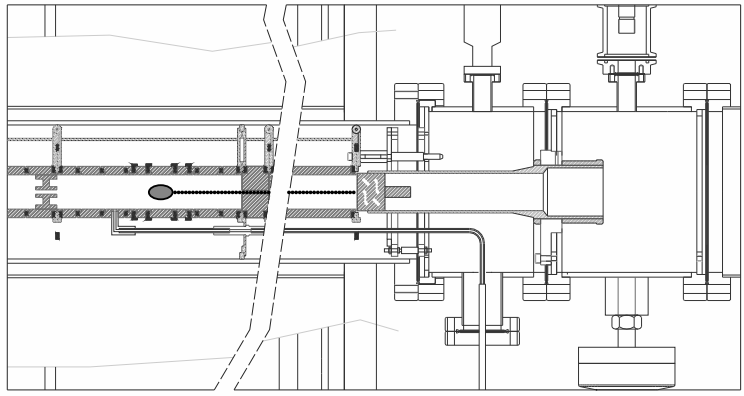

Figure 3.21: In-trap detector set-up in JYFLTRAP. The distance from the source to the detector is a little over 60 cm.

4 Results and discussion

4.1 Mass measurements

The mass of a nucleus provides information on the underlying nuclear structure. The needed accuracy depends on the phenomena to be probed. For example a mass determination accuracy of the order of 100 keV is enough to resolve global correlations such as shell closures in the mass surface. This is also the typical level of accuracy the global mass models can reach [40]. Therefore one could claim that higher precision is not needed when mapping the mass surface. However, to detect local variations in mass or binding energy due to, for example, changes of deformation, accuracies of the order of 10 keV are preferred [96]. With the improving accuracies obtained with Penning traps precision mass measurements are becoming important tools in probing nuclear structure effects by using observables such as two-neutron or two-proton separation energies, shell gap energies, pairing energies as well as proton-neutron interaction energies.

4.1.1 Masses of neutron-rich zirconium isotopes

Neutron-rich nuclei in the region of zirconium (Z $\approx$ 40) are known to have rapidly changing nuclear shape when the neutron number changes from 56 to 60. In the zirconium case this has been studied by various methods ranging from the β-decay of parent yttrium nuclei [97] to prompt fission fragment γ-ray measurements [98], and from collinear laser spectroscopy [99] to mass measurements reported in [Publication 3] and ref. [100].

To see the nuclear structure effects the obtained mass data is conveniently plotted in the form of two-neutron separation energies, $S_{2n}(\mathrm{N},\mathrm{Z}) = B(\mathrm{N},\mathrm{Z}) - B(\mathrm{N}-2,\mathrm{Z})$. In this manner the obscuring odd-even staggering is filtered out and underlying changes in the nuclear structure are more visible. In Fig. 4.1 the experimental two-neutron separation energies are plotted as a function of neutron number. From this plot the shell closure at N=50 is clearly visible. The next effect is much weaker but it can be seen around N=56 in elements from rubidium to molybdenum as a change in the slope of the S_{2n} energy. In zirconium this corresponds to a doubly closed-subshell and therefore the collectivity is suppressed which can be seen also from the systematics of the first 2^+ states [101]. The next kink is around N=60 which corresponds in zirconium to the cross over of the deformed structure to become the ground state and

the extra binding it brings to the ground state. A jump can be seen at the same neutron number in the root-mean squared charge radii of zirconium and strontium determined by collinear laser spectroscopy experiments [99, 102, 103]. The development of this effect can be followed as a function of proton number. In the S_{2n} plot the data for N=60 only starts at rubidium but from there the effect of this shape change seem to become stronger when going up in Z reaching its maximum in zirconium and then fading away by molybdenum. Above Z=42 the behavior of the two-neutron separation energy becomes smooth as is expected for these transitional nuclei. The new experimental values presented in fig. 4.1 are obtained using the JYFLTRAP precision trap and are published in refs. [100, 104, 105].

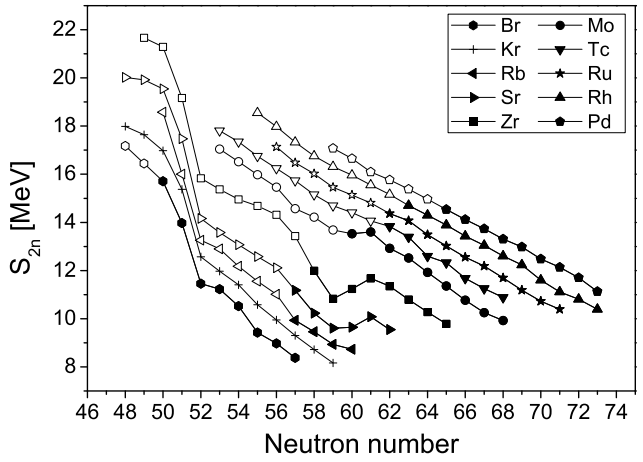

Figure 4.1: Experimental two-neutron separation energies as a function of neutron number for elements between bromine and palladium. The values measured at JYFLTRAP are marked with solid symbols, the AME03 [53] values with open symbols. The krypton chain was recently measured at ISOLTRAP [106]. The yttrium and niobium chains are left out as the analysis is not completed.

However, the first mass measurements at JYFLTRAP were performed using only the purification trap. Although it clearly has a lower resolution these measurements were carried out while the precision trap was still under construction. The masses could not be measured for atomic ions as it turned out that zirconium ions were picking up an oxygen atom becoming a monoxide ion in interactions with impurities in the buffer gas of both the cooler and the trap. Therefore the measurements were performed on monoxide ions and the reference mass was that of ^{97}ZrO. The mass of ^{97}Zr is well known, its uncertainty is

only 2.8 keV as given in the AME03 [53]. In these measurements the trapping cycle was similar to the normal purification cycle as explained in section 3.2.3 and only the frequency of the quadrupole excitation, which centers the selected ions, was scanned over the cyclotron frequency of the studied ion. The mass determination was extracted from ion counts versus excitation frequency scans, see fig. 4.2. The space charge effect was minimized by limiting the number of ions in the trap to only few at a time. For example, at REXTRAP a shift in cooling frequency due to large number of ions in the trap is reported [95] but the affect only occurs when there is more than a few 10^4 ions in the trap. The drawback of this technique is that it is sensitive to changes of incoming beam intensity as the cyclotron frequency is determined from the ion count rate. Also the presence of impurities with differing mass in the trap while exciting might affect the measured frequency. As the measured distributions could be fitted better with a function that included a possibility of an asymmetry from the statistical uncertainty could not be directly determined. Therefore a bootstrap method [107] had to be used to extract the uncertainty, see [Publication 3] for more details.

Even though the mass determination by using a cooling resonance frequency in the purification trap has its limitations, the obtained results, for example neutron-rich zirconium agree reasonably well with our new measurements using the precision trap. In fig. 4.3 the purification trap results are compared with our new precision trap results [100] by plotting a difference between our experimental mass excess values and the tabulated ones from AME03. In this figure one can see that even though the measured values for the masses of ^{102}Zr and ^{104}Zr do not agree within the error bars, the overall trend compared to the AME03 values is similar in these two set of measurements. In retrospect one could state that the uncertainties for masses of more exotic isotopes were underestimated in the first experiment. Nevertheless the first data set pointed out large deviations from the literature values and gave a much better estimate for the masses of these isotopes.

These experimental mass values can be compared to different theoretical models. For this comparison the following global mass models were selected: FRDM [43], HFB-9 [52], ETFSI-2 [44], KTUY [56], and Duflo-Zuker [55]. These are the models usually used to calculate mass values for astrophysical purposes. A brief description of these models can be found in section 2.5. In fig. 4.4 experimental two-neutron separation energies calculated from our data and those from AME2003 [53] are plotted together with these model predictions. The N=50 shell gap seen in the larger plot is nicely reproduced by almost all the models. Only the HFB-9 model seems to have some trouble in this region. However, the decreasing trend in S_{2n} starting from N=56 and the kink at N=59 is missed by the global models. All models predict a much smoother behavior except perhaps HFB-9 which has a kink at N=59 however is offset from the experimental data. In addition this model has other kinks not seen in the experimental data. It seems that, in general, the effect of the subshell closure at N=56 is underestimated in these models.

Because the global mass models fail to reproduce some of the features of the

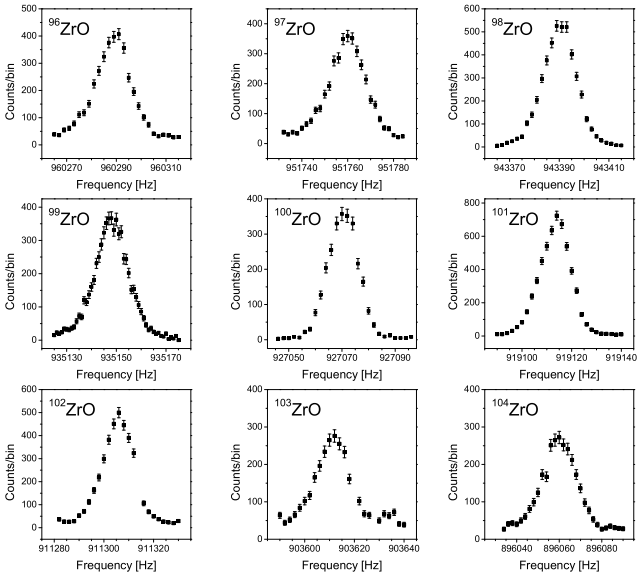

Figure 4.2: Mass scans of $^{96-104}$Zr as a zirconium monoxide. Ion counts as a function of quadrupole excitation frequency in the purification trap.

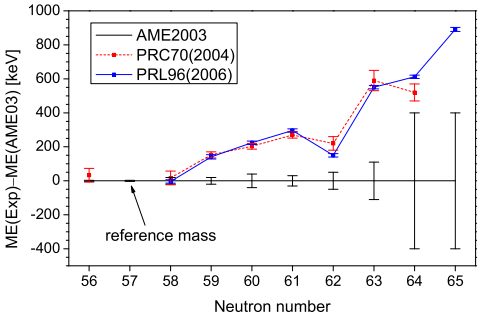

Figure 4.3: Comparison of mass excess values for zirconium isotopes measured with the purification trap and our new, more precise values from the precision trap. The plotted values are the difference between the experimental and the AME2003 values [53].

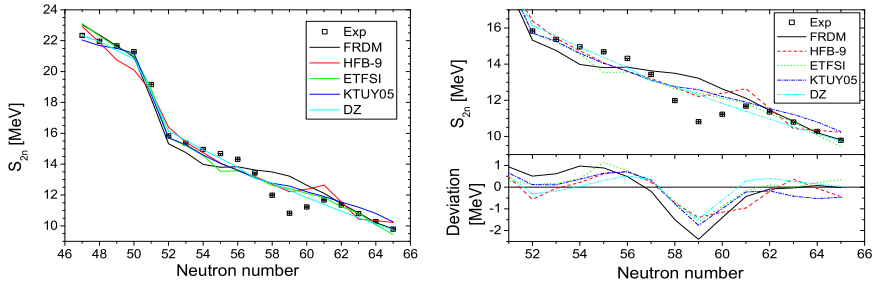

Figure 4.4: Comparison of experimental two-neutron separation energies to different model predictions. The left panel shows an overall view with the N=50 shell gap. The right panel gives a closer view of the N=60 area with model deviations from the experimental values.

mass surface around N∼60 it is interesting to see how a more dedicated local calculation performs using a truncated interacting boson model (IBM) model space does. This kind of study was carried out recently in ref. [59] partly inspired by the new mass results of the [Publication 3]. The model is inherently restricted to describe only even-even nuclei and, additionally, the neutron and proton pairs are treated as identical bosons with an effective IBM hamiltonian in order to reduce the number of model parameters. This model was then used to produce the two-neutron separation energies together with excitation energies. In fig. 4.5 the experimental two-neutron separation energies are compared with the predictions of this model. The flat behavior between A=100 and 102 is reproduced by the model and it corresponds to the rapid change from a spherical to a deformed shape seen in the energy spectra. However, the slopes before and after the flat part are not particularly well reproduced. These nuclei can also be described using configuration mixing. From that approach more insight could be gained regarding the nature of the observed shape change. More work along these lines is still needed.

4.1.2 Masses of niobium isotopes and isomers

Neutron-rich even-mass niobium isotopes ^{100,102,104}Nb are known to have two β-decaying states. No internal transition between these beta decaying states has been observed in any of the three isotopes. Previous mass determinations of these isotopes are mainly based on beta endpoint measurements, as is the excitation energy of the isomeric states. As has been noticed in many isotopic chains in this region of refractory fission products, this kind of measurement often suffers from systematic error due to insufficient knowledge of the decay schemes and unfolding of the continuous beta spectra. The measured mass excess values for zirconium, as discussed above, showed significant deviations from the literature values pointing to some errors in the Q_β-value determina-

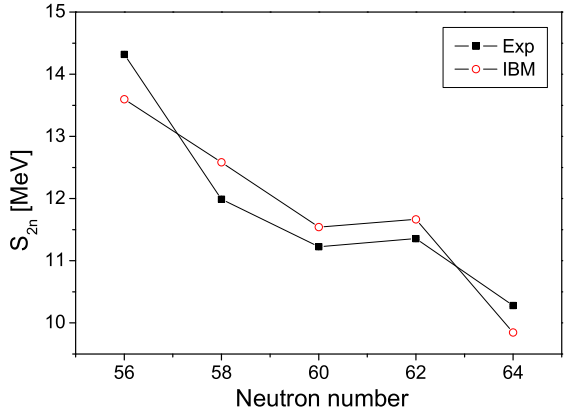

Figure 4.5: Two-neutron separation energies for even-even neutron-rich zirconium isotopes. Experimental values are plotted with solid squares, whereas interacting boson model values [59] are plotted with open circles.

tions. Therefore, it was decided to remeasure the masses of ^{100,102,104}Nb with the precision trap of the JYFLTRAP setup. This was primarily done in order to determine the Q_{β^-} values for the zirconium beta decays studied in this work. The tabulated information about the niobium beta decaying states is shown in table 4.1.

Table 4.1: The properties of beta decaying states in ^{100,102,104}Nb as tabulated in NUBASE03 [108].

Nuclide	E_{exc} [keV]	ME [keV]	$t_{1/2}$ [s]	J^π
^{100}Nb	0	-79940(26)	1.5(2)	1^+
^{100m}Nb	470(40)	-79471(28)	2.99(11)	$(4^+,5^+)$
^{102}Nb	0	-76350(40)	1.3(2)	1^+
^{102m}Nb	130(50)	-76220(50)	4.3(4)	high
^{104}Nb	0	-72230(110)	4.9(3)	(1^+)
^{104m}Nb	220(120)	-72010(100)	0.940(40)	high

The presence of isomeric states can make the mass determination more difficult. In principle the mass resolving power of the precision trap is enough to resolve states with an energy difference of a few 100 keV in this mass region

(the resolution depends on the used excitation time). However, as the resolving power of the purification trap is usually not enough to separate these states they both are injected into the precision trap. To avoid a shift of the detected cyclotron frequency due to presence of two ion species with different masses, preferably only one ion at a time should be in the trap.

The behavior of resonances when having two ion species with differing masses in the trap at the same time was studied in ref. [109]. It was trend that the magnitude of the shift in frequency of one mass increases with the number of ions having the other mass. The direction of these shifts depend on the relative separation and the half-width of the resonances. When the unperturbed resonances can not be resolved the observed resonance is narrower than the superposition of the two. However, when they are resolved they both shift towards a lower frequency.

When the isomeric and ground state are produced with the same intensity they have equally large time-of-flight effects and therefore it is easier to see two peaks in the TOF spectrum. Even then, the detected average time-of-flight effect is only half of the case with only one ion species. When one ion is on resonance the other is not and *vice versa*. However, the more probable situation is when one state is produced more abundantly than the second. In the normal TOF spectrum each point is the average time of flight of all the ions detected with that particular excitation frequency. The signal from the more weakly produced species easily falls below the visibility limit. For example, if the yield of a lesser produced species is 10 % of the total yield and the time-of-flight effect is 50 % for the case of a single ion, then the TOF effect for this more weakly produced ion is only 5 %. In this case, only with high statistics the fluctuation and error bars of individual points can be suppressed small enough to see a significant signal. Furthermore, one has to bear in mind that preferably only one ion should be in the trap at a time leading to very long measurement times in order to accumulate enough statistics.

If the cyclotron frequencies of both the ground and the isomeric states are known it is possible to extract one of the states transversely out of the trap by using a mass selective dipole excitation with the ion's reduced cyclotron frequency. As the resonance frequencies are probably rather close to each other a gaussian amplitude modulation for the exciting field would be preferable to avoid side bands. The excitation time and the amplitude must be selected so that only the ions in the selected state are cleaned away. Again better resolution requires a longer excitation with a lower amplitude. However, at the time of the niobium mass measurement the capability to do this kind of isomeric cleaning did not yet exist. The control program and the hardware were only recently upgraded to include this option.

There are also other ways of looking at the collected data to probe the more weakly populated state rather than plotting the average time of light against excitation frequency. Even if this does not provide a means to quantitatively determine the cyclotron frequency, it can point towards a region of frequency in which the search should be concentrated. The weakly produced isomeric state can be made visible in the precision trap data by looking at a time-of-flight

gated counts versus frequency plot. For gating, the time-of-flight of a typical in-resonance ion is used. In fig. 4.6 the second resonance, which is seen weakly in the TOF vs frequency plot, is clearly visible when gating the detected counts with the time-of-flight between bins 320 and 520. As the baseline counts of the main component between the bins 520–1000 are subtracted away the resonant ions show up as peaks in the spectrum.

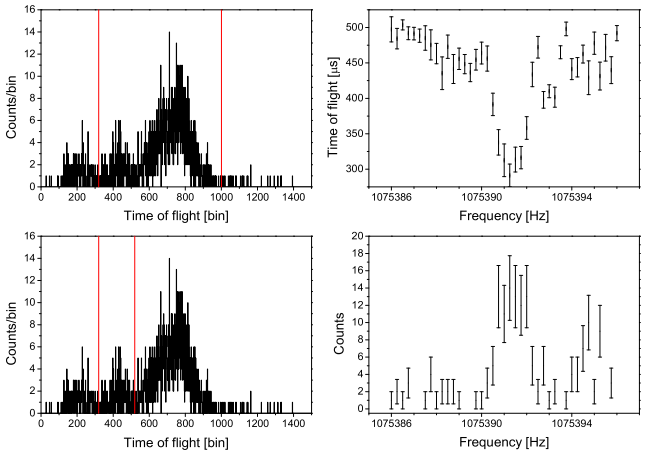

Figure 4.6: The effect of selecting a time-of-flight gating window presented by using ^{100}Nb data from one of the scans. Vertical lines drawn in the upper left spectrum show a normal gating window overbins 320–1000. The resulting average time-of-flight resonance is shown on the right. The lower left spectrum shows a gate (bins 320–520) that accepts only ions in resonance with the exciting field. On the lower right the resulting ion counts versus frequency spectrum is shown. In this last spectrum the resonant counts related to the ground state are clearly visible on the right of the main component originating from the isomeric state. The bin width is 640 ns.

As the ground and excited isomeric states usually have different half-lives one way of favoring one state over the other is to delay the measurement. To utilize this idea one can introduce the terms *direct measurement cycle* which means the normal cycle timing without any additional delays and *delayed measurement cycle* in which the ions are deliberately kept in the purification trap for some time before releasing them to the precision trap. In the case of the studied niobium isotopes this method was used with a 4 s delay to distinguish between the two states.

As the mass measurement results are discussed in more detail in [Publication 4] only a summary is given here. The masses of the niobium isotopes were first

measured by JYFLTRAP in 2004. At that time the excited isomeric and ground states could not be resolved and only one resonance per isotope was obtained. In the second experiment in 2006 ^{100}Nb, ^{102}Nb and ^{104}Nb were given special attention. Different excitation times, scanning ranges and delayed cycles were tried in order to make the two states visible. In all of these scans the ion rate was kept low to have preferably only one or two ions in the trap at the same time. For the analysis usually a maximum of 2 ions at a time was selected as the statistics for only one ion at a time was insufficient. Time-of-flight resonance spectra for all three isotopes with direct and delayed measurement cycles are shown in fig. 4.8. For the mass determination ^{97}Zr was used as a reference ion. Its tabulated mass excess is -82946.6(2.8) keV [53].

The systematic fluctuations during this experiment were determined from the measured set of the reference ion's cyclotron frequency. A value of $3 \cdot 10^{-8}$ was obtained and due to its random nature it was added to the uncertainty of each measurement. Because the reference and measured ion are not the same mass, a mass-dependent uncertainty has to be taken into account. It has been derived from the comparison of O_2 and ^{129}Xe cyclotron frequencies to be $7 \cdot 10^{-10}$ per mass unit difference. This mass-dependent uncertainty is $2.1 \cdot 10^{-9}$, $3.5 \cdot 10^{-9}$ and $4.9 \cdot 10^{-9}$ for ^{100}Nb, ^{102}Nb and ^{104}Nb, respectively. A count rate class analysis to derive the count rate dependent uncertainty could not be performed, due to low statistics. However as there were two ion species with close, but differing masses, in the precision trap at the same time, an additional uncertainty of 10^{-7} was introduced. This uncertainty dominates the uncertainty of the stronger component. The uncertainty of the weaker component comes mainly from the low statistics resulting in a larger uncertainty in the fitted position.

Mass of ^{100}Nb

In the ^{100}Nb TOF spectra a strong resonance can be seen at frequency ν_C = 1075391.26 Hz. Another weak component is at ν_C = 1075394.89 Hz. In the upper direct measurement spectrum of the fig. 4.8 a) the fit gave 1:0.15 as the intensity ratio at the moment of measurement for the two states. In the delayed measurement the ratio was 1:0.3. The goodness of the fits can be judged from the χ^2/DoF values of 1.16 and 0.98 for direct and delayed measurement, respectively. Two resonances were fitted to all collected spectra. The mass excess obtained for the excited isomeric state is -79488 ± 10 keV, which is in agreement with previous experimental data. For the ground state a mass excess of -79802 ± 20 keV was obtained leading to 313±23 keV energy difference between these states. In the delayed measurement the relative intensity of the ground state increases. Because the ground state is the shorter-lived of the two states this is against what one would expect. However there is not enough statistics to tell if this change is significant or not. Here we have to mainly rely on previous experimental data [110] in assigning the ground state spin as 1^+.

Mass of ^{102}Nb

The direct TOF spectra of ^{102}Nb look asymmetric whereas the delayed TOF is quite symmetric. In the asymmetric spectra a better fit is obtained with two resonances as compared to just one. Also by looking at the counts versus frequency plot gated by the resonant ion's time-of-flight as shown in fig. 4.7 a clear peak appears at the low frequency side of the main component. By fitting two resonance curves to the direct measurement data a better agreement with the fit is obtained than by fitting just one curve, χ^2/DoF is 1.31 compared to 1.75, respectively. The intensity ratio of these two components in the direct measurement was 1:0.15. For these two states mass excess values of -76309 ± 10 keV and -76216 ± 20 keV were derived. As the higher energy state disappears by delaying the measurement we assign the ground state as the longer-living high spin state. The obtained energy difference between these states is 93±23 keV.

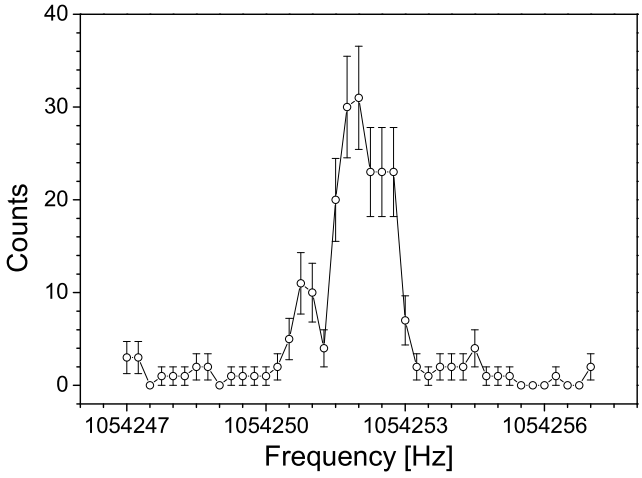

Figure 4.7: Time-of-flight gated counts versus frequency for ^{102}Nb. A second component with a lower frequency is visible. The selected gate is bins 320–550.

Mass of ^{104}Nb

The TOF spectra of ^{104}Nb shows only one component and the position of this resonance stays unchanged in the delayed measurement. As the high spin state in ^{104}Nb has only 0.94 s half-life there are very few ions left after a 4 s delay. Therefore the observed resonance is assigned for the longer living low spin state. The obtained mass excess for this state is -71823 ± 10 keV.

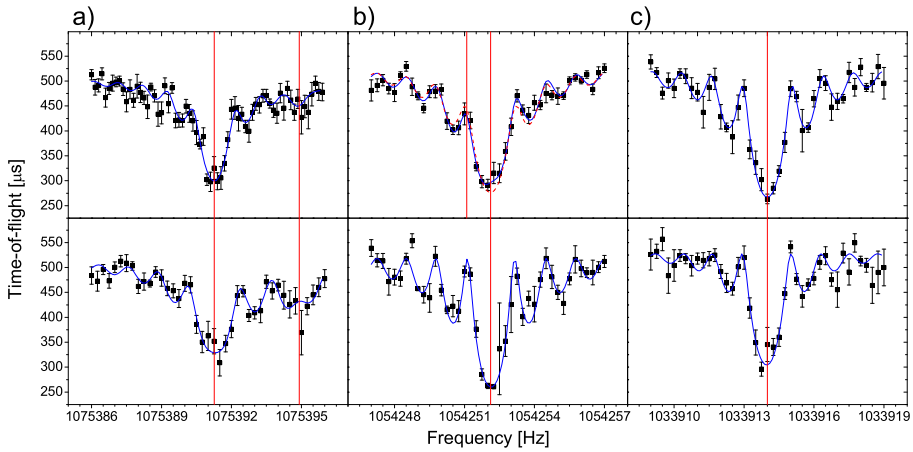

Figure 4.8: Resonance time-of-flight spectra of ^{100}Nb, ^{102}Nb and ^{104}Nb from left to right. The upper panel is the direct and lower the 4 s delayed measurement cycle. The used excitation time was 800 ms except for the direct cycle of ^{100}Nb which was measured with a 1 s excitation time. a) In ^{100}Nb two resonance positions are marked with vertical lines. The ground state is in the higher frequency as it corresponds to a lower mass. b) In the ^{102}Nb direct measurement data two separate fits were done. The dashed line is fit to one and the solid line to two resonance curves. Again the two fitted resonance positions are marked with vertical lines. c) In ^{104}Nb only one resonance peak was fitted.

4.1.3 Niobium Q_β values

As the previous experimental mass values were mostly derived from beta endpoint measurements it is interesting to compare the data as Q_β-values. The obtained niobium mass data can be converted to Q_β-values by using the masses of the daughter molybdenum isotopes [100, 53]. In fig. 4.9 these Q_β values are compared. In our first set of measurements only one resonance could be resolved for all three cases. In the new measurement with two cycle times a second state could be assigned for ^{100}Nb and ^{102}Nb. For the former of these the Q_β value of the higher energy isomeric state seems to agree with the previous value [53] but for the ground state our value is somewhat larger than the old value. For ^{102}Nb even though the Q_β value of the excited isomeric state agrees with previous value our new spin assignment changes the order of these states. Therefore the Q_β value of the 1^+ state is $\sim$145 keV higher and the high-spin state $\sim$75 keV lower than in the literature. In the case of ^{104}Nb we saw only one state whose Q_β value is 200 keV higher than that given earlier for the excited isomeric state. In most of the cases where the values disagree earlier experiments give a smaller Q_β-value than our new measurement. This could be seen as an indication of missed feeding to the higher-lying states in these beta endpoint measurements

leading to an underestimation of the deduced Q_β-values.

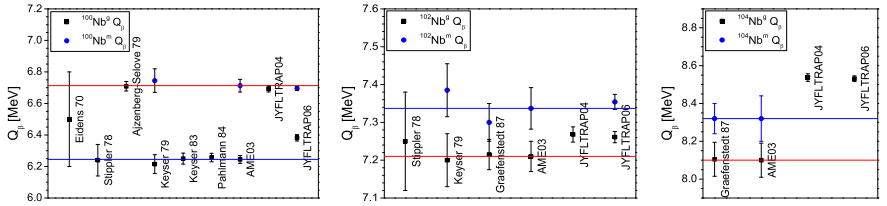

Figure 4.9: Comparison of the earlier Q_β values to our new values from mass measurements. The horizontal lines are AME03 values. The earlier data is from following references [110, 111, 112, 113, 114, 115].

4.2 Decay of neutron-rich zirconium isotopes

The neutron-rich zirconium nuclei above A=100 are strongly deformed as was discussed earlier in connection with the mass measurements. One way of probing the nuclear structure behavior related to this deformation is to study the β-decay properties of these nuclei. The behavior of the Gamow-Teller distribution can be used to judge whether the nucleus is oblate or prolate. In the region of neutron-rich zirconium nuclei the low-lying GT-strength is predicted to consist of many small peaks for oblately deformed nuclei whereas for prolate nuclei the strength is concentrated to only a few states [33].

To study the β-decay of neutron-rich zirconium isotopes the purification trap was used to produce a pure sample containing only one species of a single isotope. The γ-rays following the β-decay were recorded with detector set-ups presented in section 3.3.2. As the implanted source consists of purely zirconium nuclei the daughter activity will only grow in due to the decays of the implanted mother nuclei. When the production yield is roughly constant and the activity is not removed from the set-up the contribution of each generation of daughter activity to the total detected activity can be calculated. From this the number of β-decays belonging to the implanted parent nuclei can be deduced. The number of zirconium β-decays can be used to derive the absolute intensities for the transitions and also to provide information on the ground state branching. The derivation of these equations is presented in appendix 5.

4.2.1 β-decay of ^{100}Zr

The energies and intensities of the γ-rays assigned to this decay are listed in table 4.2 together with the observed coincident γ-rays. Two strongest transitions observed are at 504 keV and 401 keV. Gating with those peaks we see nothing in coincidence with the 504 keV transition but gating with the 401 keV transition shows coincidences with the 104 keV, 254 keV and 303 keV transitions as

reported earlier. Also the 498 keV and 704 keV peaks are observed. The placing of the former transition in the level scheme 4.10 is based only on an earlier work [116]. The energy of the latter peak equals the sum of the 303 keV and 401 keV transitions. The 695 keV peak is seen but as there is a transition with the same energy in the ^{100}Nb decay it can not be placed unambiguously in this decay scheme. An uncertain 197 keV transition in the previous work was not seen. Otherwise our data agrees with the earlier data. In addition to the previously known transitions, we could assign two new transitions (471 keV and 33 keV) to the decay of ^{100}Zr based on their identification from X-ray coincidences. In the gamma spectrum gated with the niobium K_α X-rays at 16.6 keV we find strong 401 keV and 471 keV transitions. Gating with the 471 keV transition results in a clear 33 keV peak together with the 16.6 keV X-ray peak pointing to a high conversion coefficient for the 33 keV transition. From the fluorescence production a conversion coefficient $\alpha_K = 3.1(8)$ can be deduced. In the compilation of Band *et al.* [117] α_K for a 33 keV $M1$ transition is 4.78(8), for $E1$ 2.46(4), and for $E2$ 31.7(5). A coincidence spectrum of the 33 keV transition shows only one strong peak at 471 keV. The order of the 33 keV and 471 keV transitions is based on the intensities assuming a total conversion coefficient of $\alpha = 3.5$ for the 33 keV transition. The transition energies sum up to 504 keV which agrees with the 504 keV 1^+ level energy.

The ground-state β feeding was determined to be 45(4) %. Other strongly fed states are at 504 keV and 401 keV with the log ft values of 4.49(6) and 4.79(7), respectively. Based on their strong beta feeding, a 1^+ assignment is adopted for these levels.

Because the 103.7 keV transition is between two 1^+ states it is most likely of the $M1$ type. Its theoretical [117] internal conversion coefficient $\alpha = 0.2039(29)$ leads to a total intensity $I_{\gamma+ce} = 1.10(10)$. Since other observed transitions have higher energy, their internal conversion is less probable and it has been omitted in the intensity calculation. The decay scheme showing the total transition intensities and logft values is shown in fig. 4.10.

4.2.2 β-decay of ^{102}Zr

The observed γ-transition intensities and energies listed in table 4.3 were used together with the earlier reported data [118] to produce a decay scheme of ^{102}Zr shown in fig. 4.11. The strongest transitions in this decay have energies of 64 keV, 535 keV, and 599 keV. They form a similar pattern as in the isotone ^{100}Y and are proposed to be related to the K^π=1^+ bands [119].

X-ray fluorescence was used to determine conversion coefficients when possible. For the 20.4 keV transition we deduced $\alpha_K = 7.9 \pm 2.5$ which points to $E1$ ($\alpha_K^{th} = 9.0 \pm 0.3$) or at most $M1$ ($\alpha_K^{th} = 20.0 \pm 0.6$). Similarly, for the 64.5 keV transition we obtained $\alpha_K = 0.78 \pm 0.16$ which is in agreement with the $M1$ assignment ($\alpha_K^{th} = 0.686 \pm 0.021$). The $M1$ nature of the transition also agrees with a tentative spin and parity assignment of 2^+ for the $x + 64$ keV state in [119]. We assume that the 20.4 keV transition has an $E1$ multipolarity and use the theoretical $\alpha_{tot} = 10.3$ to deduce its total intensity. According to

Table 4.2: Gamma-ray transition energies and intensities belonging to the decay of ^{100}Zr.

E_γ[keV]	$I_\gamma^\dagger$	Coincident transitions
33.01(10)	0.26(5)	471
103.73(10)	0.91(8)	401
253.3(5)	0.12(6)	401
303.8(8)	0.16(6)	401
400.81(8)	20.5(25)	104, 253, 304
471.48(9)	3.4(4)	17, 33
498.08(25)	0.80(15)	
504.37(8)	30(4)	-
704.10(33)	0.58(14)	-

† absolute intensity per 100 decays

this selection, the $x + 20.4$ keV state would have a negative parity and therefore it can only have weak direct beta feeding. For other low energy transitions an $M1$ multipolarity was assumed in conversion coefficient assignment. As the 447 keV transition was not seen in coincidence with the 156 keV transition it was not placed in the decay scheme. The Gamow-Teller strength to low-lying states is mostly shared between the $x + 599$ keV state and the $x + 0$ keV state. The spin and parity assignment of these states is therefore 1^+.

4.2.3 β-decay of ^{104}Zr

The observed transitions are listed in table 4.4 and the decay scheme of ^{104}Zr as deduced from this work and ref. [120] is shown in fig. 4.12. The first two excited states fed in the ^{104}Zr decay lie at very low energies, 8.5 keV and 37.4 keV. Internal conversion is dominant, in particular in the case of the 8.5 keV transition we see no peak with this energy in the gamma spectrum. Furthermore, as the K conversion is energetically forbidden mostly L conversion takes place. However, due to the detection threshold, L X-rays at 2.2 keV could not be seen. Evidence for this transition arises from the energy differences of transitions de-exciting higher-lying levels. The total intensity of this transition is deduced with the assumption that there is no direct beta feeding to this state. An $E1$ nature was adopted for the conversion coefficient calculation.

The second excited state at 37.4 keV de-excites via converted 28.8 keV and 37.4 keV transitions. The fluorescence yield could not be used in this case as there are two converted transitions from the same state and also due to limited statistics. Assuming the 37.4 keV transition to be $M1$ and the 28.8 keV transition to be $E1$, and no beta feeding to the lowest excited state leads to a ground state feeding of 76(6) % and log ft = 4.8. In turn, this leads to a tentative spin and parity assignment of 1^+ for the ground state. The same

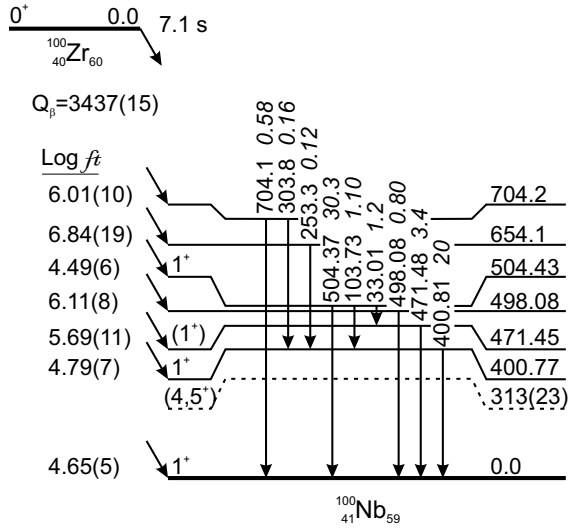

Figure 4.10: The decay scheme of ^{100}Zr. The intensities given are $I_{\gamma+ce}$ per 100 β decays. The 313 keV level drawn with a dashed line is the excited isomeric state, whose energy is based on our mass measurement. The upper limit of the ground state feeding upper limit is deduced as 45(4) %. Taken from [Publication 4].

assumptions give a log ft of 5.7 for the 37.4 keV state and a tentative $J^\pi = 1^+$ assignment.

The 514 keV state is also quite strongly fed with log $ft \approx 5.6$. In the previous literature the 250 keV and 311 keV states have been tentatively assigned as 1^+. This assignment is based on JOSEF on-line separator data given in ref. [119], and the observation of a similar band in the isotone ^{102}Y. Based on our new data, these states are not as strongly fed but rather have log $ft \approx 6.2$ and ≈ 6.4, respectively. These do not support 1^+ assignments.

4.2.4 β-decay Q-values of ^{100,102,104}Zr isotopes

As discussed in sec. 4.1 the masses of the zirconium isotopes from $A = 98$ to 105 were measured in this work [100]. By combining this data with our new mass measurements of niobium isotopes precise Q_β values for zirconium decays can be determined. In table 4.5 the new Q_β values are compared to the literature values. The Q_β-value of ^{104}Zr is measured for the first time as the earlier reported value was based on the systematic trends. All the new values

Table 4.3: Gamma-ray transition energies and intensities belonging to the decay of ^{102}Zr.

E_γ[keV]	I_γ[†]	Coincident transitions
20.38(9)	0.56(11)	74, 86, 102, 136, 152, 225
64.46(13)	8.56(10)	86, 96, 270, 458, 535, 641, 876
73.58(14)	1.17(14)	17, 152, 458
85.59(12)	0.7(3)	64, 96, 458
96.4(5)	1.1(2)	64, 86, 270, 458
102.02(17)	1.37(15)	136, 156
136.35(22)	1.4(6)	20, 102
152.4(6)	0.9(4)	74, 144, 458
156.14(14)	3.4(8)	102, 442, 549
225.35(32)	0.9(3)	110, 175, 458
246.55(26)	0.55(8)	458
258.52(22)	0.68(9)	-
270.0(5)	0.26(9)	64, 96
362.9(4)	0.9(3)	17, 64, 136, 157
442.3(5)	0.5(2)	17, 47, 64, 136, 156
458.69(21)	1.1(4)	64, 74, 86, 96, 152, 225, 247
535.13(9)	10.7(10)	64
549.0(5)	1.6(5)	
599.48(9)	13.9(13)	-
641.2(8)	0.6(2)	64
875.8(8)	0.6(2)	64
940.6(4)	1.1(2)	-

[†] absolute intensity per 100 decays

are somewhat larger than the literature values. In the case of ^{100}Zr the new mass excess of the mother nucleus is 319 keV and the daughter 137 keV higher than their AME03 values. This leads to 91 keV difference in these Q_β values. For A=102 the difference between the new and tabulated mass excess values of the mother and daughter nuclei are 150 keV and 41 keV, respectively. As again the shifts are to the same direction the resulting difference of 109 keV in the Q_β value is seen. In the case of ^{104}Zr the mass of the daughter is measured for a long-lived 1^+-state if it is the ground or the isomeric state remains an open question.

4.3 β-decay of 1^+ states in ^{100,102,104}Nb

A manifestation of two β decaying states in ^{100}Nb can be deduced from fig. 4.13 by comparing two γ spectra measured with the frequency gates in the

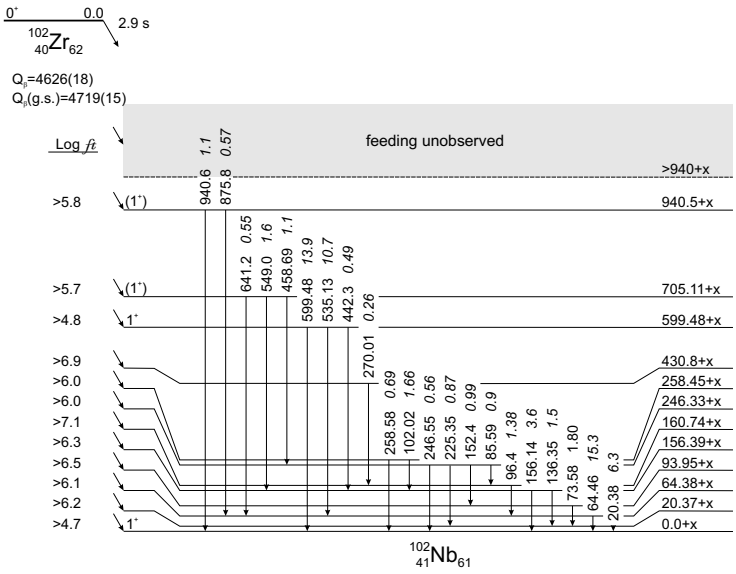

Figure 4.11: The decay scheme of ^{102}Zr. The given intensities are $I_{\gamma+ce}$ per 100 β decays. Based on our mass measurement the energy offset x is 93 ± 23 keV. The ground state feeding upper limit is deduced as 59(3) %. Taken from [Publication 4].

purification trap for ^{100}Zr and ^{100}Nb. In the upper spectrum following the ^{100}Zr decay there are, besides the peaks belonging to zirconium decay (marked with arrows), few peaks following the decay of ^{100}Nb 1^+ -state. Obviously the peaks belonging to the zirconium decay are missing from the second spectrum collected with the ^{100}Nb gate but also some new transitions appear in this spectrum. These transitions marked with an asterisk belong to the β-decay of a high spin state of ^{100}Nb produced directly in fission.

The selectivity of the allowed β-decay of the zirconium isotopes can be used here to study the β-decay of the 1^+ -states of the even-niobium isotopes. The assignment of transitions to the the 1^+ state decay is based on the assumption that the high-spin state is not populated in the β-decay of zirconium. The energy assignments of the low spin states were already discussed in the sec. 4.1.2.

4.3.1 ^{100}Nb

In the literature separate decay schemes exist for both decaying states [116]. In table 4.6 the obtained energies and intensities of the gamma transitions belonging to the decay of ^{100}Nb 1^+ ground state are listed. The third column shows the literature values for intensities.

Table 4.4: Gamma-ray transition energies and intensities belonging to the decay of ^{104}Zr.

E_γ[keV]	I_γ[†]	Coincident transitions
8.5(3)	0.8(3)*	
28.81(10)	1.3(3)	83, 157, 213, 263
37.37(10)	1.5(3)	83, 214, 263, 274
61.03(13)	1.05(14)	142, 203, 214, 243
100.94(10)	4.6(4)	141, 202, 211, 263
141.10(12)	2.0(2)	61, 101, 263
202.49(14)	1.9(2)	61, 101, 157, 213, 242, 274
210.1(3)	1.8(3)	101
212.5(3)	3.7(3)	38, 61, 202, 263
241.82(11)	3.0(3)	61, 263
250.3(7)	0.9(2)	
263.47(10)	5.2(5)	38, 101, 141, 213
274.4(3)	1.4(3)	38

† absolute intensity per 100 decays
* estimation assuming no beta feeding and E1 nature

Table 4.5: New Q_{β^-} values of Zr $\rightarrow$ $Nb_{g.s.}$ compared to the tabulated ones from ref. [53].

Isotope	Q_β[keV]	AME03 Q_β [keV]
^{100}Zr	3426±23	3335±25
^{102}Zr	4719±15	4610±30
^{104}Zr	6095±15	5880±410*

*value and uncertainty derived from systematic trends

4.3.2 ^{102}Nb

The following transitions are assigned in the literature [118] to the decay of a 1^+ state of ^{102}Nb: 296.0 keV, 397.6 keV, 400.6 keV, 551.4 keV, 847.4 keV and 949.0 keV. There exist no previous data on intensities of these transitions. We could see all but the 397.6 keV transition from the source produced in the decay of ^{102}Zr. The obtained energies and intensities for these transitions are given in table 4.7.

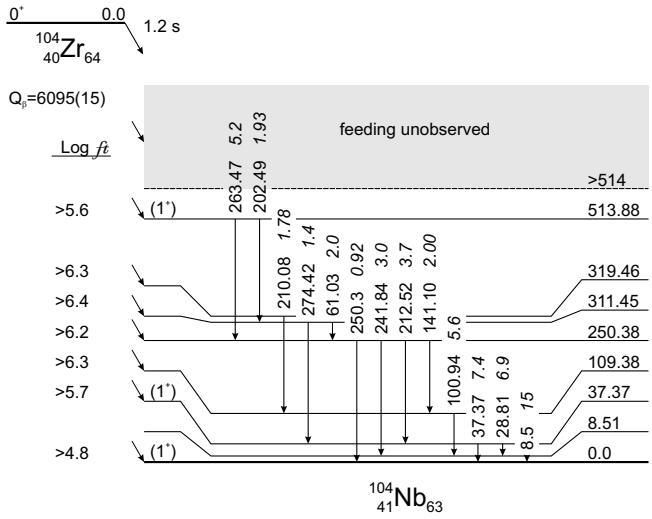

Figure 4.12: The decay scheme of ^{104}Zr. The given intensities are $I_{\gamma+ce}$ per 100 β decays. The ground state feeding upper limit is deduced as 76(6) %. Taken from [Publication 4].

4.3.3 ^{104}Nb

The decay scheme the previous works give for ^{104}Nb is a mixture of the 0.91 s and 4.8 s states [120]. Some of the transitions are listed there as only belonging to the decay of a short half-life, high-spin state according to their time behavior. These are the 368.4 keV, 477.5 keV, 519.2 keV, 555.3 keV and 771.4 keV transitions. The transitions at 192.2 keV, 620.2 keV, 693.9 keV, 812.4 keV, and 836.3 keV were fitted with mixed half-lives of 0.91 s and 4.8 s in the previous work [120].

From our study only the three transitions given in table 4.8 could be confidently assigned to the decay of the low-spin niobium state. The observed transitions agree with the earlier spin and parity assignments as they are depopulating low-spin 0^+ and 2^+ states in ^{104}Mo.

4.4 In-trap conversion electron spectroscopy

In-trap spectroscopy is thought to be exciting because of the concept of an ideal source that it can provide. Here the ideal source means a cloud of source nuclei floating almost freely in a well defined volume in the space. When a Penning trap is used for confining the source ions the magnetic field offers also an efficient transport of charged particles, in particular lower energy electrons, to the detector that can be placed further away from the source.

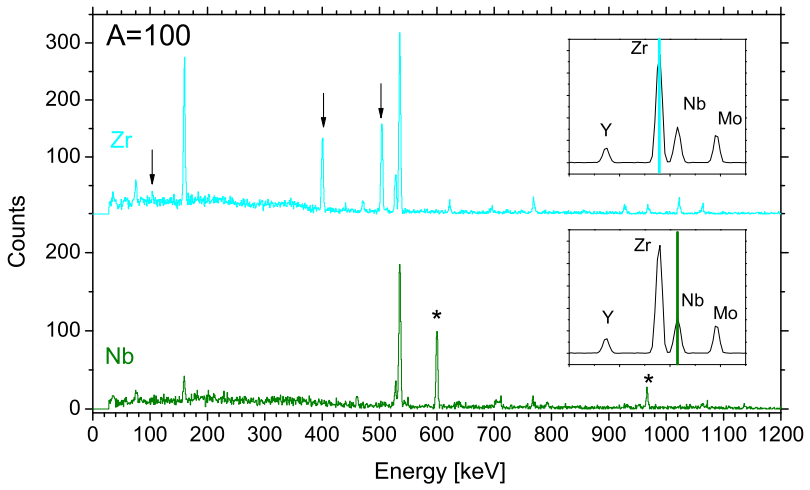

Figure 4.13: β-gated γ spectra from mass $A = 100$ ^{100}Zr gate set in trap upper panel gate ^{100}Nb lower panel. Inserts show gate position in the mass scan. See text for explanation.

4.4.1 REXTRAP results

The first feasibility tests of in-trap conversion electron spectroscopy are explained in [Publication 1] in more detail. Here only a summary is given. The following tests were done at REXTRAP. First the detector performance was tested with implanted ^{131}Ba, ^{133}Ba and ^{207}Bi sources without a magnetic field. Then the ^{131}Ba source and detector were placed inside the REXTRAP magnet to the positions where they would be in the actual on-line run. This was done to determine the transport efficiency of electrons through the magnetic field.

The electron transport efficiency was also simulated by using a SIMION code [121]. In these simulations a finite source size, a tilted incident angle affecting the back scattering from the detector and edge effects were considered. The effective thicknesses of the dead layer and the detector itself were also taken into account. The simulated transport efficiency was folded with the internal efficiency of the detector found in the first test, and the resulting total efficiency was compared with the experimental efficiency determined in the second test, see fig. 4.14.

For the first on-line test the trap settings were first tuned with the help of a MCP placed after the trap. Then the trap was vented and the detector placed in the trap. For the on-line test beams of ^{116}In and ^{118}In were produced from a uranium carbide target of ISOLDE. The studied converted transitions were

Table 4.6: Gamma-ray transition energies and intensities belonging to the decay of a 1^+ state of ^{100}Nb. The third column gives the literature value for the intensity [116].

E_γ[keV]	I_γ[†]	I_γ[‡]
159.56(2)	17.9(15)	10.7
441.06(12)	1.2(2)	1.07
528.31(5)	12.2(14)	9.1
535.63(4)	62(7)	46
574.0(5)	0.40(8)	0.29
600.53(9)	2.2(3)	0.55
622.72(9)	2.4(3)	1.5
768.92(7)	5.3(7)	3.4
928.41(8)	4.2(5)	2.5
968.97(8)	4.36(5)	2.6
1022.71(7)	8.0(10)	4.9
1063.90(11)	0.46(13)	3.3
1071.3(7)	0.50(14)	0.49
1257.2(2)	1.3(2)	0.9
1281.5(4)	0.66(12)	0.14
1502.25(10)	7.0(9)	4.4
1550.7(3)	1.2(2)	0.68
1654.0(2)	1.9(3)	1.23
1873.6(7)	0.41(15)	0.33
1908.3(7)	0.42(15)	0.39
2434.9(3)	2.2(5)	1.39
2532.9(4)	0.54(12)	0.81

† absolute γ intensity per 100 decays
‡ absolute $\gamma + ce$ intensity per 100 decays

from the second isomeric states of these indium nuclei ^{116m2}In and ^{118m2}In. The spectra collected from the decay of these sources are shown in fig. 4.15. One can see in them the K conversion peaks at 134.5 keV and 110 keV and L together with unresolved M conversion peaks at 158.2 keV and 134 keV for ^{116m2}In and ^{118m2}In, respectively. The peak resolution was not as good as with a solid source but partly it was affected by the laser ion source causing electronic noise. Another reason is thought to be the strong atomic electron background which is summed with the conversion electrons arriving at the detector simultaneously. This view is supported by the fact that the resolution and the background gets worse in the spectrum of ^{118m2}In which was 4 fold more intensive. The peak at 60 keV is caused by the stray electrons accelerated from the ground potential by the potential difference of 60 kV.

Table 4.7: Gamma-ray transition energies and intensities belonging to the decay of a ^{102}Nb 1^+ state.

E_γ[keV]	I_γ[†]
296.1(1)	70(5)
401.0(1)	17(2)
551.2(1)	11(2)
847.5(2)	6(1)
948.9(3)	3(1)

† absolute intensity per 100 decays

Table 4.8: Gamma-ray transition energies and intensities belonging to the decay of a ^{104}Nb low spin (1^+) state.

E_γ[keV]	I_γ[†]	Initial state I^{π}[‡]
192.2(1)	29(4)	2^+
620.2(2)	2.3(8)	$1, 2^+$
693.2(2)	2.2(8)	0^+

† absolute intensity per 100 decays
‡ from ref. [120]

In a later off-line experiment with a trapped α-decaying ^{221}Fr source an $E2$ transition in its daughter ^{217}Ac was studied. The source nuclei were produced in decays of long-lived activities in a used target, from where they were extracted by heating to 2000°C. In this case there was a strong low energy (less than 50 keV) background introduced as a new feature in the spectra. From a solid ^{221}Fr source this kind of low energy background was not observed. Therefore, it has to be related to some low energy phenomenon that is not visible with solid source. One option is the recoiling daughter nuclei that have of the order of 100 keV energy after the α-decay. However an efficient transport would require a higher charge state for the ion which may be realized through a shake-off process following the decay. Other observation from this experiment was a confirmation of the earlier suspicion that the increasing number of ions in the trap degrades the resolution and line shape.

4.4.2 JYFLTRAP results

Again the performance of the detector was first checked using a ^{133}Ba electron source first without a magnetic field and then placing the source inside the trap electrode structure in the magnetic field. Because the detector assembly does

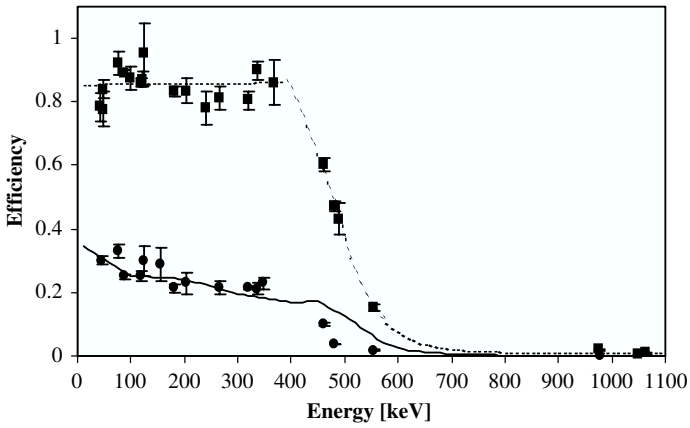

Figure 4.14: Experimentally determined internal efficiency is plotted with squares and the fit to these points with dashed line. This fit folded with a simulated electron transport efficiency yielded a calculated total efficiency drawn with the solid line. Experimentally determined efficiency using an implanted source in a trap is plotted with circles. Figure is taken from [Publication 1].

not fit into the electrode structure of JYFLTRAP it was placed as close as possible to the end of the electrode stack. This time the implanted source was not placed in the location of the trapped on-line source but only about 5 cm away from the detector. As expected the peak resolution became slightly worse when the source was placed in the magnetic field. For the on-line experiment the source was removed and the trap settings were tuned with stable beam using the FC in front of the detector. In this on-line experiment altogether 10 sources were produced in a proton induced fission of a natural uranium target. Most of the selected cases were isomeric states deexciting by emission of one or more conversion electrons. These source ions were held in the purification trap. The loading of the ions in the JYFLTRAP is done dynamically by lowering the injection side potential wall as explained in the section 3.2.3. When the wall is lowered for an injection of a new bunch the previous bunch is ejected towards the RFQ. After the capture a mass selective cooling was performed for each bunch and only then the acquisition was started to collect data on electrons emitted only by the selected ions. The cycle time *i.e.* the time each bunch was held in the trap varied between 50 and 2000 ms depending on the half-life. The results discussed here are included in the manuscript we have prepared for publication [122].

A conversion electron spectrum of an isomer ^{117m}Pd with a shortest half-life ($t_{1/2}$ = 19.1 ms) of the measured ones is shown in fig. 4.16 a). The peak at 155 keV is assigned as a sum peak of the K-conversion electrons of 35 keV and 169 keV transitions. This shows how efficient the electron transport from the source

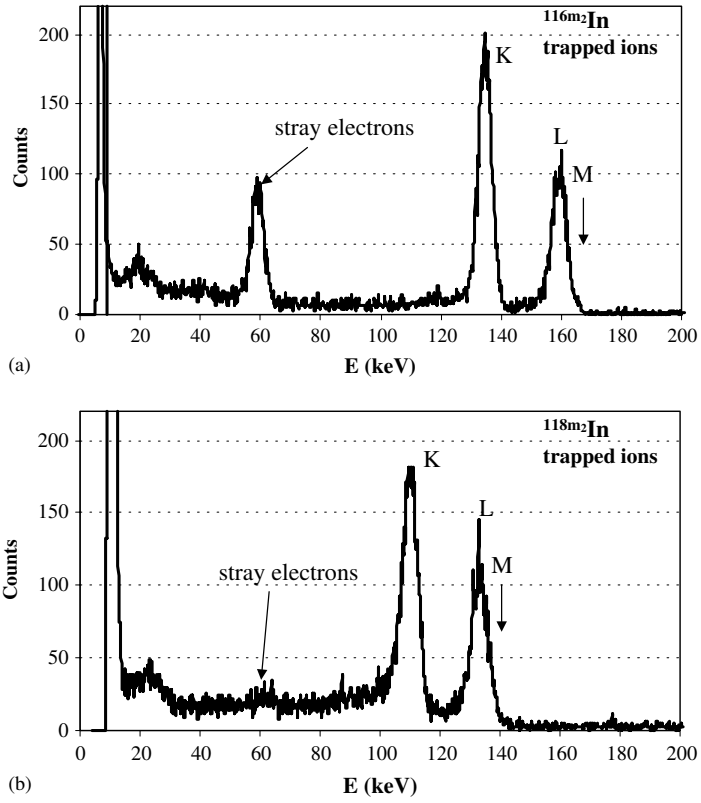

Figure 4.15: Conversion electron spectra. (a) is collected from ^{116m2}In trapped isomers and (b) is collected from ^{118m2}In trapped isomers. Figure is taken from [Publication 1].

to the detector is. For comparison, also the same ^{118m2}In isomeric state was measured as in the first test at REXTRAP, see fig. 4.16 b). The detected peak resolution 2.3 keV was better than in the previous experiment at REXTRAP. However, the production rate was much smaller than at ISOLDE leading to smaller amount of ions in the trap at a time. This reduces the probability of accidental summing with atomic electrons. Because the beam is decelerated from 30 keV energy already before the RFQ, background peaks caused by the stray electrons accelerated from ground potential are not seen.

The magnetic field at the distance of the detector reduces from 7 T at the trapping region to only 0.7 T. This large change in the field strength reduces the transport efficiency of higher energy electrons. In particular, the transport efficiency is very sensitive to the radial displacement of the source ion in the trap. Partly due to less efficient transport the total number of counts in the

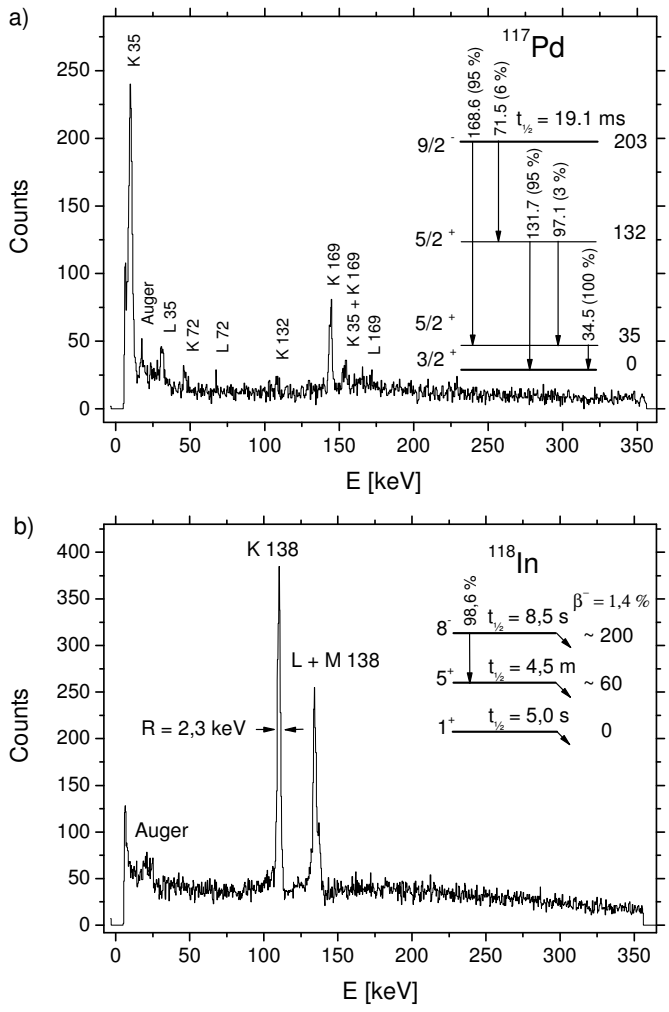

Figure 4.16: a) An electron spectrum collected from a trapped ^{117m}Pd isomer source. The decay scheme is from ref. [123]. b) A spectrum collected from ^{118m2}In trapped isomers. The decay scheme is from [26]. The picture is taken from ref. [122].

spectra were much lower than in the REXTRAP case even though much longer accumulation times were used.

4.5 Discussion

The masses of neutron-rich zirconium isotopes, now measured with high precision, can be used to reveal the nuclear structure changes as moving along the isotopic chain. As discussed earlier in sec. 4.1 it is convenient to plot derivatives of the mass values rather than the actual mass values that vary rapidly as a function of N and Z. The two-neutron separation energy has proven to be very efficient when looking nuclear structure effects along an isotopic chain. The experimental zirconium mass data was already presented in this form and compared with theoretical models, see fig. 4.4. Here another derivative, a three-point filter $\Delta_{\mathrm{N}}^{(3)}$ introduced in ref. [124], is used to extract pairing energies. The three-point filter is defined as

$$\Delta_{\mathrm{N}}^{(3)} = \frac{(-1)^{\mathrm{N}}}{2}\left[B(\mathrm{Z},\mathrm{N}-1) + B(\mathrm{Z},\mathrm{N}+1) - 2B(\mathrm{Z},\mathrm{N})\right] \tag{4.1}$$

where $B(\mathrm{Z},\mathrm{N})$ is the negative binding energy. In fig. 4.17 experimental $\Delta_{\mathrm{N}}^{(3)}$ are compared to five model predictions [43, 54, 44, 56, 55] for the same quantity. Again the magic shell closure at N=50 is giving the largest signal. Theoretical models reproduce the shell closure rather nicely. Also the general odd-even staggering is well visible in predictions. However, the subshell closure at N=56, reflected as a high point at N=56 and following low value in N=57, is once more disregarded by the models. The inverse staggering of the N=59 point is predicted only by HFB-9.

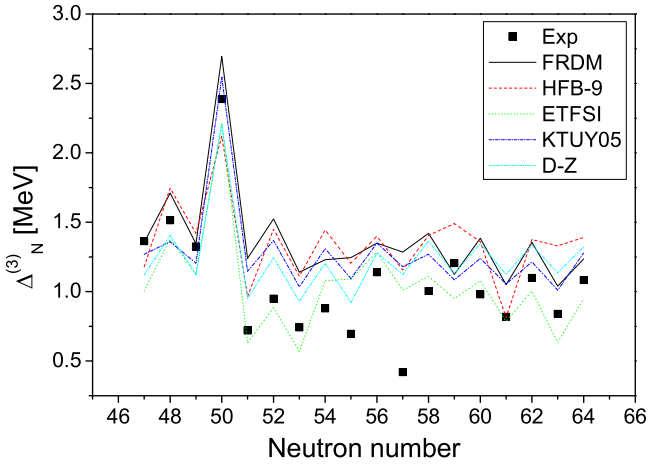

Figure 4.17: Experimental pairing energy calculated using three-mass formula compared to five different models. The values for N<58 are from ref. [53].

As a result of the zirconium decay study β branchings could be determined. By combining those with the Q_β-values obtained from the mass measurements, Gamow-Teller strengths for the transitions were derived. The obtained Gamow-Teller strength distributions of zirconium isotopes can be compared to their lighter strontium isotones, see figs. 4.18–4.20. In the case of ^{100}Zr and ^{98}Sr the strength peaks at 500 keV and 600 keV, respectively. In the decay of ^{100}Zr the observed feeding ends at 700 keV whereas in ^{98}Sr it goes up to 1900 keV. However the GT strength to these high-lying states in yttrium is not very strong. The transitions deexciting the high-lying states in yttrium proceed via low energy states, and therefore, are in coincidence with these low energy transitions. In zirconium decay the spectra collected in coincidence with the known low energy transitions did not show any stronger higher energy transitions. However, in the case of the strontium decay transitions deexciting the highest levels are rather weak and probably the low statistics in ^{100}Zr decay limited detection of those weak transitions at higher energy. Furthermore, as the Q_β value of ^{100}Zr is only 3.4 MeV compared to 7.1 MeV in ^{98}Sr the same GT strength into a high-lying level in zirconium would result in a smaller beta branching than in strontium.

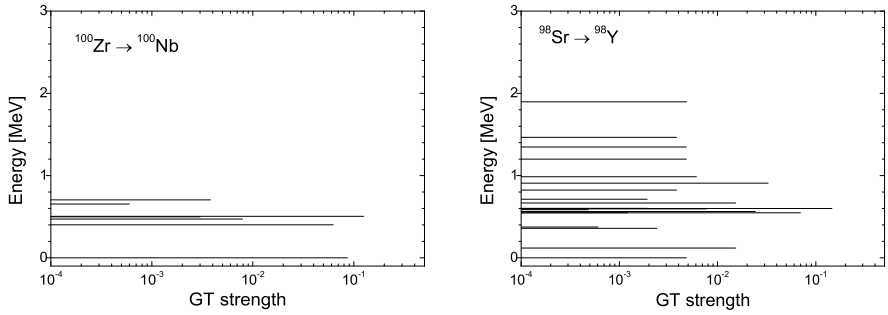

Figure 4.18: Observed GT-strengths in the case of ^{100}Zr decay. The second graph shows a similar plot for ^{98}Sr as a comparison. The strontium data is from ref. [125].

In ^{102}Zr decay (fig. 4.19) the energy axis is shifted by 93 keV due to the excitation energy of the 1^+ isomeric state. The GT-strength of ^{102}Zr decay is peaked in two levels as in the ^{100}Sr decay. The observed distribution ends again at lower energy in zirconium than in the strontium decay. Two sensitivity limits drawn on top of the ^{102}Zr data shows a 2σ peak detection limit in a β-gated γ-spectrum and in a 250 keV γ-gated spectrum. The first one sets the limit to detect a transition but to assign the transition to the decay of ^{102}Zr it has to be seen in coincidence with some of the already known transitions. The γ-gated sensitivity limit is giving the idea of a GT-strength needed to see the transition in coincidence with other γ transition.

The GT-strength distribution of ^{104}Zr differs from the ^{102}Sr one as even

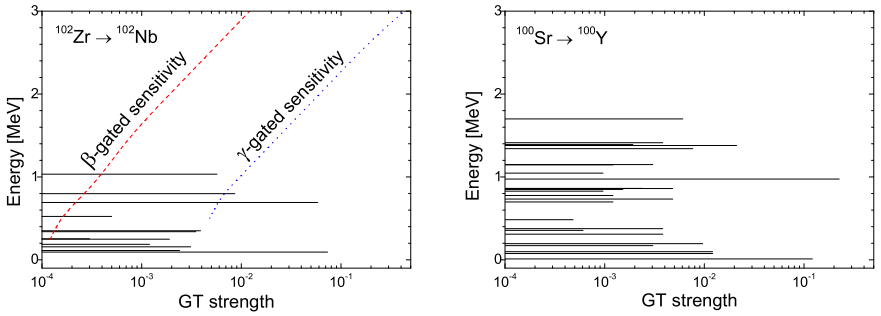

Figure 4.19: Observed GT-strengths and detection sensitivity limits in the case of ^{102}Zr decay. Detection sensitivity limits are estimated for 2σ peaks. The γ-gated detection limit is calculated assuming coincidence with a 250 keV transition. The second graph shows a similar plot for ^{100}Sr as a comparison. The strontium data is from ref. [116].

though the low-energy part is rather similar. Strontium decay feeds strongly two yttrium levels around 1.5 MeV but in the zirconium decay similar feeding is not observed. Partly this is due to sensitivity limit, as can be deduced from the sensitivity limits drawn in the graph. However feeding as strong as observed in the strontium decay should be visible also in zirconium. Unless the feeding goes to levels higher in energy than in the case of strontium.

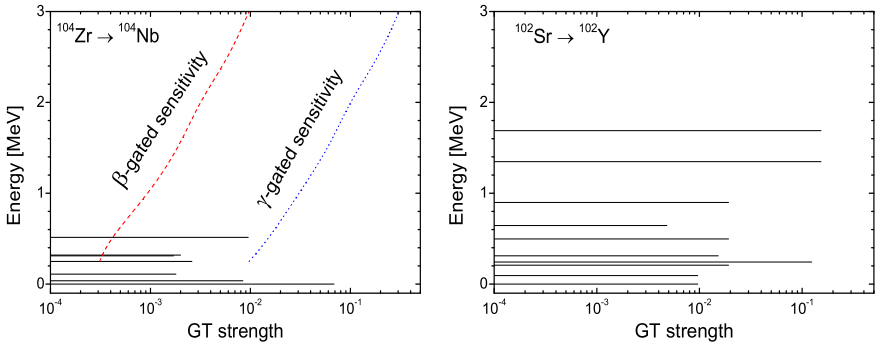

Figure 4.20: Observed GT-strengths and detection sensitivity limits in the case of ^{104}Zr decay. Detection sensitivity limits are estimated for 2σ peaks. The γ-gated detection limit is calculated assuming coincidence with a 250 keV transition. The second graph shows a similar plot for ^{102}Sr (two protons lighter isotone of ^{104}Zr) as a comparison. The strontium data is from ref. [118].

To summarize, the higher Q_β-values for strontium isotopes open larger win-

dow for the beta decay but otherwise there are similarities in the distributions. Quite likely there is also a missed feeding in ^{102}Zr and ^{104}Zr decays as indicated in the decay schemes. In fact, a comparison of the total GT-strength B_σ(GT) (fig. 4.21) reveals a drop in the case of zirconium isotopes when adding neutrons whereas the trend is increasing in the strontium isotopes after N=60. This could be taken as an indication of missed feeding in the decays of ^{102}Zr and ^{104}Zr. All in all, the experimental GT-strength distributions seem to be concentrated to only few states. Similar behavior is earlier seen in some neutron-rich even molybdenum isotopes [126, 127]. According to Skyrme type Hartree-Fock calculations employing Tamm-Dancoff Approximation or random phase approximation performed by Urkedal *et al.* [33] the Gamow-Teller strength is distributed between many weak transitions for nuclei in this region if the nucleus is oblately deformed whereas prolate deformation leads to only few strong transitions. Based on this our results would suggest a prolate deformation for the studied zirconium nuclei.

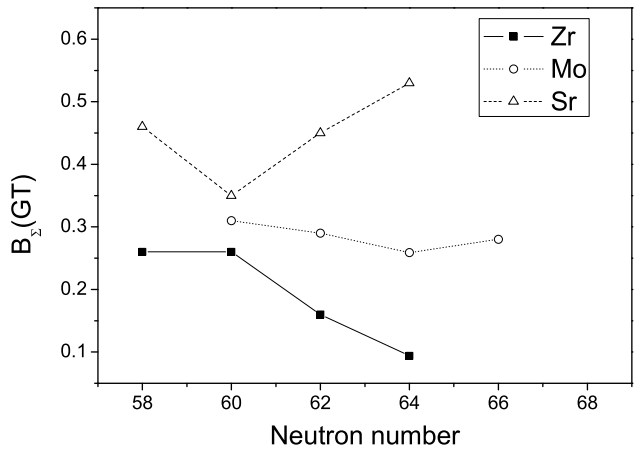

Figure 4.21: Observed total GT-strengths for zirconium, molybdenum and strontium isotopes. The strontium and molybdenum data are from refs. [128, 125, 116, 118, 126].

Using the selectivity of the β-decay in populating levels with different spins, a source of low-spin niobium state can be created from the zirconium 0^+ state decay. This way the γ-transitions following the decay of the low-spin state of niobium isotopes could be studied. However, as this was already outside of the focus of this work only a list of γ-ray energies and intensities for each isotope was made. The assignment on these transitions to the decay of niobium isotopes was based on previous data [116, 118, 120].

The in-trap conversion electron spectroscopy tests proved the principle of de-

tecting electrons with high efficiency and with improved line shape quality. The application of the technique is not limited only to nuclear spectroscopy but also diagnostics of trapped ion bunches can be realized and if the detector resolution would allow also atomic data could be extracted. Therefore, to get the most out of the ideal source the detector resolution should be still improved. In addition, with the expense of a small size the detector could be pulled further out from the magnetic field making the electrons incident angle closer to perpendicular and thus reducing the backscattering and energy loss in the detector dead layer. The summing of coincident electrons could be reduced by use of pixel detector which would also enable collection of coincidence data. This technique could be utilized also in the decay study of zirconium isotopes. As it was found out in the performed γ-spectroscopy experiments there are many highly converted low-energy transitions in these decay schemes. More information on these decays might be obtained by conversion electron spectroscopy with low energy detection threshold and good line shape quality that the in-trap spectroscopy can offer.

5 Summary and outlook

This work was centered around ion trapping techniques and their different applications. During this work a double Penning trap system was built at the IGISOL facility at the University of Jyväskylä. In this work the Penning trap was used to determine atomic masses of short-lived neutron-rich zirconium and niobium isotopes and isomers. However the main emphasis was on trap-assisted spectroscopy. For this the trap was utilized as a high resolving power mass separator to provide clean sources for decay spectroscopy of ^{100}Zr, ^{102}Zr and ^{104}Zr. Furthermore a feasibility of an in-trap conversion electron spectroscopy was tested in Penning traps at ISOLDE, CERN and at Jyväskylä.

The use of a clean zirconium source provided by the purification trap enabled precise determination of the absolute intensities of γ-transitions following the β-decay. From these intensities the β branchings and furthermore the GT-strength distributions could be determined by inclusion of newly measured Q_β-values. Of the Q_β values the one for ^{104}Zr was experimentally determined for the first time. The obtained GT-strength distribution would suggest prolate deformation for these zirconium nuclei based on the calculations in ref. [33]. The possible missed feeding to high lying states – the Pandemonium effect [129] – prevented determination of the absolute ft values for decays of ^{102}Zr and ^{104}Zr therefore only lower limits could be given. To overcome this limitation higher yields are required. To reduce the daughter activity originating background the collection tape could be moved every $\sim$10 s. This would reduce the duty cycle but at the same time it would increase the ratio of zirconium decays to daughter decays bringing the transitions following zirconium decay more visible in the spectra. Also the detection method using a high resolution and low efficiency germanium detectors could be replaced with a high efficiency low resolution total absorption spectrometer. In particular as the purification trap can be used to deliver a clean source.

The zirconium decay experiment can be seen as a commissioning experiment for the isobarical purification with JYFLTRAP. Following this, few other experiments have already been performed with purified beams. As the isotopic purity is necessary in many spectroscopic applications, it is foreseen that a significant part of the future experiments at IGISOL will be performed using the isobaric purification mode of JYFLTRAP. In-trap spectroscopy tests proved the potential this method might have in terms of high precision and sensitivity.

Following the development of Penning traps becoming a standard tool for

study of radioactive nuclei, new ways of utilizing the special properties that they can provide for the low energy radioactive ion beams have started to come up. For the atomic mass determination of short lived nuclei Penning traps have been used already for 20 years [130]. Since then they were also used for beam bunching and later on Penning traps have been used for beam purification. Purification traps were in a natural way first utilized in mass measurement experiments already using Penning traps. The JYFLTRAP was the first trap project that was designed for both mass measurements and being a preparatory stage for decay spectroscopy.

In the decay spectroscopy at IGISOL the isobaric background has become the main limitation when pushing the studies further from stability towards very exotic neutron-rich nuclei produced in fission. As in these exotic nuclei the fission yields drop about one order of magnitude for each step in the isobaric chain away from the stability the small signal from the studied nucleus is easily swamped by the huge background. In most isotopic chains the limit has been reached where a standard decay spectroscopy experiment with β-trigger and γ-detectors alone could resolve the one neutron more exotic isotope. In order to proceed from here the ISOL beam needs to be further purified with a Penning trap. When the beta branchings are of interest it is convenient to have a pure sample of only one nuclide species as discussed in relation to zirconium decay spectroscopy. In the case of the superallowed $0^+ \rightarrow 0^+$ beta emitters extremely precise branching ratio and half-life measurements are needed. Therefore, these experiments could also benefit from a purified source. Some spectroscopy techniques are particularly vulnerable for contaminant activity. For example, in total absorption spectrometry (TAS) the nuclear information has to be extracted from the experimental data by rather complicated analysis in which a contaminant activity is difficult to handle. To derive convincing data out of these TAS experiments the possibility to use isobarically clean beam would be a great advantage. The purification does not have to be limited to only isobaric level but with higher resolving power also isomeric states can be separated [131]. This would also open interesting new possibilities for the decay spectroscopy.

Dedicated devices are also designed and build for in-trap decay studies. However, they are often aimed to study one particular phenomenon for example beta-neutrino correlation like in the case of WITCH [7]. Therefore a need for general purpose decay spectroscopy device for in-trap decay studies still exists. Further development of in-trap detector systems is also needed to fully utilize the potential of the ideal source that has come available with application of trapping techniques. Something could be learned from other fields as nuclear physics is not the only field doing in-trap detection of emitted radiation. In fact, traps deviced with detectors are for example used in high energy physics to study antimatter. Slowed down antiprotons and positrons are carefully brought together in a nested Penning trap to form antihydrogen. Annihilation at trap wall following the escape of neutral antiatom from the trap is detected with gamma and charged particle detectors surrounding the trap [132, 133]. Some ideas from the detectors used in these experiments could be transferred to nuclear spectroscopy. As the high magnetic field inside a Penning trap does not allow

use of germanium detectors, scintillator material like CsI, BaF, $LaBr_3$(Ce) with photodiode or light guide readout could be used for gamma detection around the trapping region. Also dedicated charged particle detectors could be placed inside the trap. The different magnetic rigidities of emitted charged particles could be used to separate them to their specific detectors. A schematic view of how this kind of in-trap detector system for a Penning trap could look like is shown in fig. 5.1.

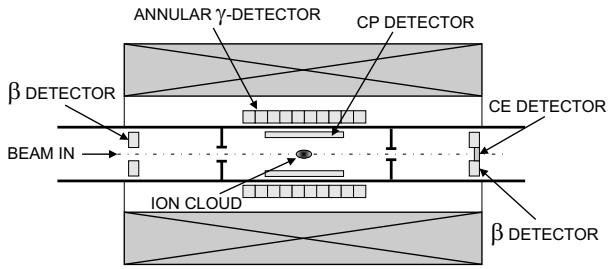

Figure 5.1: Detector set-up for advanced in-trap spectroscopy including detectors for low energy conversion electrons, beta particles, other charged particles (protons, alphas) and gammas.

Of course there is no need to limit the in-trap spectroscopy considerations only to Penning traps. As it was pointed out in the introduction optical traps are widely used in experiments in close contact to nuclear physics [6, 4, 5]. Also a Paul trap and an electron beam ion trap, which can be operated without an electron beam as a Penning trap, are suggested for in-trap spectroscopy as the access to the trapping region is not blocked by a magnet coil [8, 134].

The future of trap-assisted spectroscopy looks bright. From the present facilities JYFLTRAP is ready and equipped for decay spectroscopy with purified beams and ISOLTRAP is making preparations to install a tape station and detector set-up behind the trap. From the near future projects TITAN at TRIUMF, Vancouver is becoming operational soon and also there preparations for in-trap spectroscopy experiments are done. The designs of the future large nuclear physics facilities like FAIR [135], SPIRAL2 [136], EURISOL [137], and RIA [138] include Penning traps not only for mass measurements but also for trap-assisted spectroscopy as it is seen as a technique of the future. To summarize, the trap-assisted spectroscopy is now taking the first steps but within coming years it probably becomes a standard method to study very exotic nuclei with high precision.

Appendix

Ground state branching calculation

The number of decays belonging to zirconium was determined by using the decay law

$$A = A_0 e^{-\lambda t} \tag{A-1}$$

Generally for activity at time t we have equation

$$A(t) = \lambda N(t) = P(1 - e^{-\lambda t}), \tag{A-2}$$

where λ is decay constant, N is number of radioactive atoms, and P is production rate of atoms (beam intensity). Now we consider a decay chain where a radioactive isotope 1 is produced with a constant rate P and it decays to next radioactive isotope 2 that again decays to 3 and so on. The decay rate of these isotopes are characterized by their own specific decay constants λ_1, λ_2, ... (or half-lives $t_{1/2}$). An initial condition of no activity at time $t = 0$ can be also placed as the collection tape is moved before the implantation starts. For activity 1 simple equation

$$A_1(t) = \lambda_1 N_1(t) = P(1 - e^{-\lambda_1 t}) \tag{A-3}$$

can be written. For its daughter activity 2 the following differential equation can be derived

$$\frac{dN_2}{dt} + \lambda_2 N_2(t) = \lambda_1 N_1(t) = P(1 - e^{-\lambda_1 t}). \tag{A-4}$$

Solution for this type of differential equation is

$$N_2 e^{\lambda_2 t} = \int (P e \lambda_2 t - P e^{(\lambda_2 - \lambda_1)t}) dt + C = \frac{P}{\lambda_2} e^{\lambda_2 t} - \frac{P}{\lambda_2 - \lambda_1} e^{(\lambda_2 - \lambda_1)t} + C \tag{A-5}$$

Applying the initial condition $N_2 = 0$ when $t = 0$ we get

$$C = \frac{P}{\lambda_2 - \lambda_1} - \frac{P}{\lambda_2}. \tag{A-6}$$

Substituting this to the eq A-5 one gets

$$N_2(t) = \frac{P}{\lambda_2}(1 - e^{-\lambda_2 t}) + \frac{P}{\lambda_2 - \lambda_1}(e^{-\lambda_2 t} - e^{-\lambda_1 t}). \tag{A-7}$$

Similarly for isotope 3 we get differential equation

$$\frac{dN_3}{dt} + \lambda_3 N_3(t) = \lambda_2 N_2(t) = P(1 - e^{-\lambda_2 t}) + \frac{\lambda_2 P}{\lambda_2 - \lambda_1}(e^{-\lambda_2 t} - e^{-\lambda_1 t}) \tag{A-8}$$

and by solving this N_3 can be obtained

$$\begin{aligned} N_3(t) &= P\Bigg[\frac{1}{\lambda_3}(1 - e^{-\lambda_3 t}) \\ &\quad - \frac{1}{\lambda_3 - \lambda_2}(e^{-\lambda_2 t} - e^{-\lambda_3 t}) \\ &\quad + \frac{\lambda_2}{(\lambda_2 - \lambda_1)(\lambda_3 - \lambda_2)}(e^{-\lambda_2 t} - e^{-\lambda_3 t}) \\ &\quad - \frac{\lambda_2}{(\lambda_2 - \lambda_1)(\lambda_3 - \lambda_1)}(e^{-\lambda_1 t} - e^{-\lambda_3 t})\Bigg] \end{aligned} \tag{A-9}$$

For two of the studied masses also isotope 4 decay is needed. The differential equation for it is

$$\frac{dN_4}{dt} + \lambda_4 N_4(t) = \lambda_3 N_3(t), \tag{A-10}$$

in which one can substitute $N_3(t)$ with result from equation A-9 and solve it.

$$\begin{aligned} N_4(t) &= e^{-\lambda_4 t} P\Bigg[\frac{1}{\lambda_4}(e^{\lambda_4 t} - 1) \\ &\quad - \frac{1}{\lambda_4 - \lambda_3}(e^{(\lambda_4 - \lambda_3)t} - 1) \\ &\quad - \frac{\lambda_1 \lambda_3}{(\lambda_2 - \lambda_1)(\lambda_3 - \lambda_2)(\lambda_4 - \lambda_2)}(e^{(\lambda_4 - \lambda_2)t} - 1) \\ &\quad + \frac{\lambda_1 \lambda_3}{(\lambda_2 - \lambda_1)(\lambda_3 - \lambda_2)(\lambda_4 - \lambda_3)}(e^{(\lambda_4 - \lambda_3)t} - 1) \\ &\quad - \frac{\lambda_2 \lambda_3}{(\lambda_2 - \lambda_1)(\lambda_3 - \lambda_1)(\lambda_4 - \lambda_1)}(e^{(\lambda_4 - \lambda_1)t} - 1) \\ &\quad + \frac{\lambda_2 \lambda_3}{(\lambda_2 - \lambda_1)(\lambda_3 - \lambda_1)(\lambda_4 - \lambda_3)}(e^{(\lambda_4 - \lambda_3)t} - 1)\Bigg] \end{aligned} \tag{A-11}$$

Now we have time dependence of the number of nuclei for all isotopes. The total number of decays for all isotopes can be obtained by integrating activity over the measuring time.

$$D_1 = \int_0^T A_1 dt = \int_0^T P(1 - e^{-\lambda_1 t})dt = P\left[T + \frac{1}{\lambda_1}(e^{-\lambda_1 T} - 1)\right] \qquad \text{(A-12)}$$

In a similar way, D can be obtained for other activities.

Bibliography

[1] G. Bollen, S. Becker, H.-J. Kluge, M. König, R. Moore, T. Otto, H. Raimbault-Hartmann, G. Savard, L. Schweikhard, H. Stolzenberg, ISOLDE Collaboration, Nucl. Instrum. Methods Phys. Res. A **368**, 675 (1996).

[2] G. Marx, D. Ackermann, J. Dilling, F. Hessberger, S. Hoffmann, H.-J. Kluge, R. Mann, G. Mnzenberg, Z. Qamhieh, W. Quint, D. Rodriguez, M. Schdel, J. Schnfelder, G. Sikler, C. Toader, C. Weber, O. Engels, D. Habs, P. Thirolf, H. Backe, A. Dretzke, W. Lauth, W. Ludolphs, M. Sewtz, Hyperfine Int. **132**, 459 (2001).

[3] G. Bollen, S. Schwarz, D. Davies, P. Lofy, D. Morrissey, R. Ringle, P. Schury, T. Sun, L. Weissman, Nucl. Instrum. Methods Phys. Res. A **532**, 203 (2004).

[4] N. Scielzo, S. Freedman, B. Fujikawa, P. Vetter, Phys. Rev. Lett. **93**, 102501 (2004).

[5] A. Gorelov, D. Melconian, W. Alford, D. Ashery, G. Ball, J. Behr, P. Bricault, J. D'Auria, J. Deutsch, J. Dilling, M. Dombsky, P. Dubé, J. Fingler, U. Giessen, F. Glück, S. Gu, O. Häusser, K. Jackson, B. Jennings, M. Pearson, T. Stocki, T. Swanson, M. Trinczek, Phys. Rev. Lett. **94**, 142501 (2005).

[6] S. Crane, S. Brice, A. Goldschmidt, R. Guckert, A. Hime, J. Kitten, D. Vieira, X. Zhao, Phys. Rev. Lett. **86**, 2967 (2001).

[7] V. Kozlov, N. Severijns, D. Beck, M. Beck, S. Coeck, B. Delauré, A. Lindroth, S. Kopecky, P. Delahaye, F. Wenander, V. Golovko, I. Kraev, T. Phalet, Int. J. Mass Spectrom. **251**, 159 (2006).

[8] E. Liénard, G. Ban, G. Darius, D. Durand, X. Fléchard, M. Herbane, M. Labalme, F. Mauger, A. Mery, O. Naviliat-Cuncic, D. Rodríguez, in *Int. Conf. on Frontiers in Nuclear Structure, Astrophysics, and Reactions - FINUSTAR, Kos, Greece*, edited by S. V. Harissopulos, P. Demetriou, R. Julin (AIP) (2006), volume 831 of *AIP Conference Proceedings*, pp. 44–48.

[9] I. Tanihata, J. Phys. G: Nucl. Part. Phys. **22**, 157 (1996).

[10] A. Kraznahorkay, et al., Nucl. Phys. A **731**, 224 (2004).

[11] C. Horowitz, J. Piekarewicz, Phys. Rev. Lett. **86**, 5647 (2001).

[12] K. Langanke, G. Martínez-Pinedo, Rev. Mod. Phys. **75**, 819 (2003).

[13] J. C. F.-K. Thielemann, J. Truran, Phys. Rep. **208**, 267 (1991).

[14] B. Chen, J. Dobaczewski, K.-L. Kratz, K. Langanke, B. Pfeiffer, F.-K. Thielemann, P. Vogel, Phys. Lett. B **355**, 37 (1995).

[15] N. Schunck, J. Dudek, A. Góźdź., P. Regan, Phys. Rev. C **69**, 061305(R) (2004).

[16] G. Gamow, Proc. R. Soc. London, Ser. A **126**, 632 (1930).

[17] M. G. Mayer, Phys. Rev. **75**, 1969 (1949).

[18] O. Haxel, J. H. D. Jensen, H. E. Suess, Phys. Rev. **75**, 1766 (1949).

[19] A. Bohr, B. Mottelson, *Nuclear structure, Vol II: Nuclear deformation* (benjamin, New York) (1975).

[20] F. Iachello, A. Arima, Phys. Lett. B **53**, 309 (1974).

[21] A. Poves, E. Caurier, F. Nowacki, A. Zuker, Eur. Phys. J. **20**, 119 (2004).

[22] T. Otsuka, Hyperfine Interact. **132**, 409 (2001).

[23] S. Nilsson, Mat. Fys. Medd. Dan. Vid. Selsk. **26** (1955).

[24] B. R. Mottelson, S. G. Nilsson, Phys. Rev. **99**, 1615 (1955).

[25] R. Bengtsson, J. Dudek, W. Nazarewicz, P. Olanders, Phys. Scr. **39**, 196 (1989).

[26] R. Firestone, V. Shirley, *Table of Isotopes, 8th edition* (Wiley, New York) (1996).

[27] F.Iachello, A. Arima, *The Interacting Boson Model* (Cambridge University Press, Cambridge, England) (1987).

[28] N. Severijns, M. Beck, O. Naviliat-Cuncic, Rev. Mod. Phys. **78**, 991 (2006).

[29] B. Singh, J. Rodriguez, S. Wong, J. Tuli, Nucl. Data Sheets **84**, 487 (1998).

[30] W.-M. Yao, et al., J. Phys. G **33**, 1 (2006).

[31] J. Hardy, I. Towner, Phys. Rev. C **71**, 055501 (2005).

[32] P. Möller, J. Randrup, Nucl. Phys. A **514**, 1 (1990).

[33] P. Urkedal, X. Zhang, I. Hamamoto, Phys. Rev. C **64**, 054304 (2001).

[34] J. Suhonen, *From Nucleons to Nucleus, Concepts of Microscopic Nuclear Theory* (Springer, Berlin) (2007), to be published.

[35] M. Freedman, Ann. Rev. Nucl. Sci. **24**, 209 (1974).

[36] T. Carlson, W. Hunt, M. Krause, Phys. Rev. **151**, 41 (1966).

[37] G. Audi, Int. J. Mass Spectr. Ion Process. **251**, 85 (2006).

[38] K. Blaum, Phys. Rep. **425**, 1 (2006).

[39] D. Lunney, J. Pearson, C. Thibault, Rev. Mod. Phys. **75**, 1021 (2003).

[40] J. Pearson, S. Goriely, Nucl. Phys. A **777**, 623 (2006).

[41] C. von Weizsäcker, Z. Phys. **96**, 431 (1935).

[42] W. Myers, W. Swiatecki, Nucl. Phys. **81**, 1 (1966).

[43] P. Möller, J. Nix, W. Myers, W. Swiatecki, At. Data Nucl. Data Tables **59**, 135 (1995).

[44] S. Goriely, in *Proc. of the 10th Int. Symposium on Capture Gamma-Ray Spectroscopy and Related Topics*, edited by S. Wender (AIP) (2000), volume 529 of *AIP Conference Proceedings*.

[45] S. Goriely, Hyperfine Interact. **132**, 105 (2004).

[46] W. Myers, W. Swiatecki, Nucl. Phys. A **601**, 141 (1996).

[47] G. Lalazissis, S. Raman, P. Ring, At. Data Nucl. Data Tables **71**, 1 (1999).

[48] D. Vretenar, A. Afanasjev, G. Lalazissis, P. Ring, Phys. Rep. **409**, 101 (2005).

[49] S. Goriely, F. Tondeur, J. Pearson, At. Data Nucl. Data Tables **77**, 311 (2001).

[50] M. Samyn, S. Goriely, P.-H. Heenen, J. Pearson, F. Tondeur, Nucl. Phys. A **700**, 142 (2002).

[51] S. Goriely, M. Samyn, P.-H. Heenen, J. Pearson, F. Tondeur, Phys. Rev. C **66**, 024326 (2002).

[52] J. P. M. Onsi, S. Goriely, M. Samyn, Nucl. Phys. A **758**, 651c (2005).

[53] A. Wapstra, G. Audi, C. Thibault, Nucl. Phys. A **729**, 129 (2003).

[54] S. Goriely, M. Samyn, J. Pearson, M. Onsi, Nucl. Phys. A **750**, 425 (2005).

[55] J. Duflo, A. Zuker, Phys. Rev. C **52**, R23 (1995).

[56] H. Koura, T. Tachibana, M. Uno, M. Yamada, Prog. Theor. Phys. **113**, 305 (2005).

[57] H. Koura, M. Uno, T. Tachibana, M. Yamada, Nucl. Phys. A **674**, 47 (2000).

[58] R. Fossion, C. D. Coster, J. García-Ramos, T. Werner, K. Heyde, Nucl. Phys. A **697**, 703 (2002).

[59] J. García-Ramos, K. Heyde, R. Fossion, V. Hellemans, S. D. Baerdemacker, Eur. Phys. J. A **26**, 221 (2005).

[60] P. Dendooven, Nucl. Instrum. Methods Phys. Res. B **126**, 182 (1997).

[61] E. Kugler, Hyperfine Interact. **129**, 23 (2000).

[62] V. Mishin, V. Fedoseyev, H.-J. Kluge, V. Letokhov, H. Ravn, F. Scheerer, Y. Shirakabe, S. Sundell, O. Tengblad, Nucl. Instrum. Methods Phys. Res. B **73**, 550 (1993).

[63] U. Köster, V. Fedoseyev, V. Mishin, L. Weissman, M. Huyse, K. Kruglov, W. Mueller, P. V. Duppen, J. V. Roosbroeck, P. Thirolf, H. G. Thomas, D. Weisshaar, W. Schulze, R. Borcea, M. L. Commara, H. Schatz, K. Schmidt, S. Röttger, G. Huber, V. Sebastian, K. Kratz, R. Catherall, U. Georg, J. Lettry, M. Oinonen, H. Ravn, H. Simon, I. collaboration, Nucl. Instrum. Methods Phys. Res. B **160**, 528 (2000).

[64] http://isolde.web.cern.ch/ISOLDE/.

[65] J. Ärje, K. Valli, Nucl. Instrum. Methods **179**, 533 (1981).

[66] J. Äystö, J. Ärje, V. Koponen, P. Taskinen, H. Hyvönen, A. Hautojarvi, K. Vierinen, Phys. Lett. B **138**, 369 (1984).

[67] J. Ärje, J. Äystö, H. Hyvönen, P. Taskinen, V. Koponen, J. Honkanen, A. Hautojarvi, K. Vierinen, Phys. Rev. Lett. **54**, 99 (1985).

[68] J. Ärje, J. Äystö, H. Hyvönen, P. Taskinen, V. Koponen, J. Honkanen, K. Valli, A. Hautojärvi, K. Vierinen, Nucl. Instrum. Methods Phys. Res. A **247**, 431 (1986).

[69] J. Ärje, J. Äystö, P. Taskinen, J. Honkanen, K. Valli, Nucl. Instrum. Methods Phys. Res. B **26**, 384 (1987).

[70] J. Äystö, P. Taskinen, M. Yoshii, J. Honkanen, P. Jauho, J. Ärje, K. Valli, Nucl. Instrum. Methods Phys. Res. B **26**, 394 (1987).

[71] J. Äystö, P. Taskinen, M. Yoshii, J. Honkanen, P. Jauho, H. Penttilä, C. Davis, Phys. Lett. B **201**, 211 (1988).

[72] T. Sonoda (2006), private comm.

[73] H. Penttilä, J. Billowes, P. Campbell, P. Dendooven, V.-V. Elomaa, T. Eronen, U. Hager, J. Hakala, J. Huikari, A. Jokinen, A. Kankainen, P. Karvonen, S. Kopecky, B. Marsh, I. Moore, A. Nieminen, A. Popov, S. Rinta-Antila, Y. Wang, J. Äystö, Eur. Phys. J. A **25**, 745 (2005).

[74] P. Karvonen, T. Sonoda, I. Moore, J. Billowes, A. Jokinen, T. Kessler, H. Penttilä, A. Popov, B. Tordoff, J. Äystö, Eur. Phys. J. A (To be published).

[75] A. Nieminen, I. Moore, J. Billowes, P. Campbell, K. Flanagan, C. Geppert, J. Huikari, A. Jokinen, T. Kessler, B. Marsh, H. Penttilä, S. Rinta-Antila, B. Tordoff, K. Wendt, J. Äystö, Hyperfine Interact. **162**, 39 (2006).

[76] J. Äystö, Nucl. Phys. A **693**, 477 (2001).

[77] H. Penttilä, P. Dendooven, A. Honkanen, M.Huhta, P. Jauho, A. Jokinen, G. Lhersonneau, M. Oinonen, J.-M. Parmonen, K. Peräjärvi, J. Äystö, Nucl. Instrum. Methods Phys. Res. B **126**, 213 (1997).

[78] A. Nieminen, J. Huikari, A. Jokinen, J. Äystö, P. Campbell, E. Cochrane, Nucl. Instrum. Methods Phys. Res. A **469**, 244 (2001).

[79] A. Nieminen, P. Campbell, J. Billowes, D. Forrest, J. Griffith, J. Huikari, A. Jokinen, I. Moore, R. Moore, G. Tungate, J. Äystö, Phys. Rev. Lett. **88**, 094801 (2002).

[80] H. Dehmelt, *Advances in Atomic and Molecular Physics* (Academic Press, New York, NY), volume 3 of *Advances in Atomic and Molecular Physics*, p. 53 (1967).

[81] I. Bergström, C. Carlberg, T. Fritioff, G. Douysset, J. Schönfelder, R. Schuch, Nucl. Instrum. Methods Phys. Res. A **487**, 618 (2002).

[82] G. Bollen, R. Moore, G. Savard, H. Stolzenberg, J. App. Phys. **68**, 4355 (1990).

[83] G. Gabrielse, L. Haarsma, S. Rolston, Int. J. Mass Spectrom. Ion Proc. **88**, 319 (1989).

[84] H. Raimbault-Hartmann, D. Beck, G. Bollen, M. König, H.-J. Kluge, E. Schark, J. Stein, S. Schwarz, J. Szerypo, Nucl. Instrum. Methods Phys. Res. B **126**, 378 (1997).

[85] V. Kolhinen, S. Kopecky, T. Eronen, U. Hager, J. Hakala, J. Huikari, A. Jokinen, A. Nieminen, S. Rinta-Antila, J. Szerypo, J. Äystö, Nucl. Instrum. Methods Phys. Res. A **528**, 776 (2004).

[86] G. Savard, S. Becker, G. Bollen, H.-J. Kluge, R. Moore, T. Otto, L. Schweikhard, H. Stolzenberg, U. Wiess, Phys. Lett. A **158**, 247 (1991).

[87] K. Blaum, G. Bollen, F. Herfurt, A. Kellerbauer, H.-J. Kluge, M. Kuckein, S. Heinz, P. Schmidt, L. Sweikhard, J. Phys. B **36**, 921 (2003).

[88] M. König, G. Bollen, H.-J. Kluge, T. Otto, J. Szerypo, Int. J. Mass Spectrom. Ion Processes **142**, 95 (1995).

[89] V. Kolhinen, Ph.D. thesis, University of Jyväskylä (2003).

[90] A. Nieminen, P. Campbell, J. Billowes, D. Forest, J. Griffith, J. Huikari, A. Jokinen, I. Moore, R. Moore, G.Tungate, J. Äystö, Nucl. Instrum. Methods Phys. Res. B **204**, 563 (2003).

[91] D. Radford, Nucl. Instrum. Methods Phys. Res. A **361**, 297 (1995).

[92] J. Parmonen, Z. Janas, W. Trzaska, J. Äystö, J. Kantele, P. Jauho, A. Jokinen, H. Penttilä, Nucl. Instrum. Methods Phys. Res. A **306**, 504 (1991).

[93] J. Kantele, *Handbook of Nuclear Spectrometry* (Academic Press Ltd, London) (1995).

[94] D. Habs, et al., Hyperfine Interact. **129**, 43 (2000).

[95] F. Ames, , et al., Hyperfine Interact. **132**, 469 (2001).

[96] R. B. Cakirli, D. S. Brenner, R. F. Casten, E. A. Millman, Phys. Rev. Lett. **94**, 092501 (2005).

[97] G. Lhersonneau, P. Dendooven, A. Honkanen, M. Huhta, P. M. Jones, R. Julin, S. Juutinen, M. Oinonen, H. Penttilä, J. R. Persson, K. Peräjärvi, A. Savelius, J. C. Wang, J. Äystö, Phys. Rev. C **56**, 2445 (1997).

[98] W. Urban, J. Durell, A. G. Smith, W. Phillips, M. Jones, B. Varley, T. Rzaca-Urban, I. Ahmad, L. Morss, M. Bentaleb, N. Schulz, Nucl. Phys. A **689**, 605 (2001).

[99] P. Campbell, H. L. Thayer, J. Billowes, P. Dendooven, K. T. Flanagan, D. H. Forest, J. A. R. Griffith, J. Huikari, A. Jokinen, R. Moore, A. Nieminen, G. Tungate, S. Zemlyanoi, J. Äystö, Phys. Rev. Lett. **89**, 082501 (2002).

[100] U. Hager, T. Eronen, J. Hakala, A. Jokinen, V. S. Kolhinen, S. Kopecky, I. Moore, A. Nieminen, M. Oinonen, S. Rinta-Antila, J. Szerypo, J. Äystö, Phys. Rev. Lett. **96**, 042504 (2006).

[101] J. Wood, K. Heyde, W. Nazarewicz, M. Huyse, P. van Duppen, Phys. Rep. **251**, 101 (1992).

[102] F. Buchinger, E. B. Ramsay, E. Arnold, W. Neu, R. Neugart, K. Wendt, R. E. Silverans, P. Lievens, L. Vermeeren, D. Berdichevsky, R. Fleming, D. W. L. Sprung, G. Ulm, Phys. Rev. C **41**, 2883 (1990).

[103] P. Lievens, R. E. Silverans, L. Vermeeren, W. Borchers, W. Neu, R. Neugart, K. Wendt, F. Buchinger, E. Arnold, I. Collaboration", Phys. Lett. B **256**, 141 (1991).

[104] U. Hager, V.-V. Elomaa, T. Eronen, J. Hakala, A. Jokinen, A. Kankainen, S. Rahaman, S. Rinta-Antila, A. Saastamoinen, T. Sonoda, J. Äystö, Submitted to Phys. Rev. C (2006).

[105] S. Rahaman, U. Hager, V.-V. Elomaa, T. Eronen, J. Hakala, A. Jokinen, A. Kankainen, P. Karvonen, I. Moore, H. Penttilä, S. Rinta-Antila, J. Rissanen, A. Saastamoinen, T. Sonoda, J. Äystö, Submitted to Eur. Phys. J. A (2006).

[106] P. Delahaye, G. Audi, K. Blaum, F. Carrel, S. George, F. Herfurth, A. Herlert, A. Kellerbauer, H.-J. Kluge, D. Lunney, L. Schweikhard, C. Yazidjian, Phys. Rev. C **74**, 034331 (2006).

[107] W. Press, S. Teukolsky, W. Vetterling, B. Flannery, *Numerical Recipies in C* (Cambridge University Press, Cambridge, England) (1992).

[108] G. Audi, O. Bersillon, J. Blachot, A. Wapstra, Nucl. Phys. A **729**, 3 (2003).

[109] G. Bollen, H.-J. Kluge, M. König, T. Otto, G. Savard, H. Stolzenberg, R. B. Moore, G. Rouleau, G. Audi, ISOLDE Collaboration, Phys. Rev. C **46**, R2140 (1992).

[110] U. Keyser, H. Berg, F. Münnich, B. Pahlmann, R. Decker, B. Pfeiffer, in *Proc. 6th Int. Conf. on Atomic Masses and Fundamental Constants, East Lansing, MI, USA* (Plenum, New York) (1979), pp. 443–449.

[111] J. Eidens, E. Roeckl, P. Armbruster, Nucl. Phys. A **141**, 289 (1970).

[112] R. Stippler, F. Münnich, H. Schrader, J. Bocquet, M. Asghar, G. Siegert, R. Decker, B. Pfeiffer, H. Wollnik, E. Monnand, F. Schussler, Z. Phys. A **284**, 95 (1978).

[113] U. Keyser, F. Münnich, B. Pahlmann, B. Pfeiffer, H. Weikard, Z. Phys. A **313**, 251 (1983).

[114] B. Pahlmann, M. Grafenstedt, U. Keyser, F. Münnich, B. Pfeiffer, H. Weikard, Z. Phys. A **318**, 371 (1984).

[115] M. Graefenstedt, U. Keyser, F. Münnich, F. Schreiber, H. Faust, H. Weikard, Z. Phys. A **327**, 383 (1987).

[116] B. Singh, Nucl. Data Sheets **81**, 1 (1997).

[117] I. Band, M. Trzhaskovskaya, J. C.W. Nestor, P. Tikkanen, S. Raman, At. Data and Nucl. Data Tables **81**, 1 (2002).

[118] D. de Frenne, E. Jacobs, Nucl. Data Sheets **83**, 535 (1998).

[119] L. Peker, F. Wohn, J. Hill, R. Petry, Phys. Lett. B **169**, 323 (1986).

[120] J. Blachot, Nucl. Data Sheets **64**, 1 (1991).

[121] D. Dahl, Int. J. Mass Spectrom. **200**, 3 (2000).

[122] J. Rissanen, V.-V. Elomaa, T. Eronen, J. Hakala, A. Jokinen, S. Rahaman, S. Rinta-Antila, J. Äystö, Eur. Phys. J. A (To be published).

[123] W. Urban, A. Zlomaniec, J. Pinston, J. Kurpeta, T. Rzaca-Urban, J. Durell, A. G. Smith, B. Varley, N. Schulz, I. Ahmad, Eur. Phys. J. A **22**, 157 (2004).

[124] J. Dobaczewski, P. Magierski, W. Nazarewicz, W. Satuła, Z. Szymanski, Phys. Rev. C **63**, 024308 (2001).

[125] B. Singh, Z. Hu, Nucl. Data Sheets **98**, 335 (2003).

[126] A. Jokinen, T. Enqvist, P. Jauho, M. Leino, J. Parmonen, H. Penttilä, J. Äystö, K. Eskola, Nucl. Phys. A. **584**, 489 (1995).

[127] J. Wang, P. Dendooven, S. Hankonen, J. Huikari, A. Jokinen, V. Kolhinen, G. Lhersonneau, A. Nieminen, K. Peräjärvi, S. Rinta-Antila, J. Äystö, Eur. Phys. J. A **19**, 83 (2004).

[128] L. Peker, Nucl. Data Sheets **68**, 165 (1992).

[129] J. Hardy, L. Carraz, B. Jonson, P. Hansen, Phys. Lett. B **71**, 307 (1977).

[130] G. Bollen, P. Dabkievicz, P. Egelhof, T. Hilberath, H. Kalinowsky, F. Kern, H.-J. Kluge, R. Moore, H. Schnatz, L. Schweikhard, H. Stolzenberg, G. Temmer, G. Ulm, the ISOLDE Collaboration, Hyperfine Interact. **38**, 793 (1987).

[131] K. Blaum, D. Beck, G. Bollen, P. Delahaye, C. Guénaut, F. Herfurth, A. Kellerbauer, H.-J. Kluge, D. Lunney, S. Schwarz, L. Schweikhard, C. Yazidjian, Europhys. Lett. **67**, 586592 (2004).

[132] M. Amoretti, C. Amsler, G. Bonomi, A. Bouchta, P. Bowe, C. Carraro, C. Cesar, M. Charlton, M. J. T. Collier, M. Doser, V. Filippini, K. Fine, A. Fontana, M. Fujiwara, R. Funakoshi, P. Genova, J. Hangst, R. Hayano, M. Holzscheiter, L. Jrgensen, V. Lagomarsino, R. Landua, D. Lindelf, E. L. Rizzini, M. Macri, N. Madsen, G. Manuzio, M. Marchesotti, P. Montagna, H. Pruys, C. Regenfus, P. Riedler, J. Rochet, A. Rotondi, G. Rouleau, G. Testera, A. Variola, T. L. Watson, D. van der Werf, Nature **419**, 456 (2002).

[133] G. Gabrielse, N. Bowden, P. Oxley, A. Speck, C. Storry, J. Tan, M. Wessels, D. Grzonka, W. Oelert, G. Schepers, T. Sefzick, J. W. H. Pittner, T. Hänsch, E. Hessels, Phys. Rev. Lett. **89**, 213401 (2002).

[134] D. Frekers, J. Dilling, I. Tanihata,
http://titan.triumf.ca/research/publications/S1066_proposal.pdf.

[135] http://www.gsi.de/fair/index_e.html.

[136] http://www.ganil.fr/research/developments/spiral2/.

[137] http://www.eurisol.org/.

[138] http://www.orau.org/ria/.